CYCLOSTATIONARY STATISTICAL OPTICS

BY

ROBERT W. SCHOONOVER

DISSERTATION

Submitted in partial fulfillment of the requirements
for the degree of Doctor of Philosophy in Electrical and Computer Engineering
in the Graduate College of the
University of Illinois at Urbana-Champaign, 2010

Urbana, Illinois

Doctoral Committee:

Associate Professor P. Scott Carney, Chair
Professor J. Gary Eden
Assistant Professor Michael L. Oelze
Assistant Professor Gabriel Popescu

ABSTRACT

Pulsed, optical fields are treated theoretically within the framework of cyclostationary random processes. Propagation-induced effects for stochastic, pulsed fields that are either beam-like or plane waves are examined in the context of interferometric and spectroscopic measurements. Propagation of fields from more general sources is considered in relation to the spectral or polarimetric properties observed. A new scheme for measuring cyclostationary effects is proposed.

To Katrina

ACKNOWLEDGMENTS

I am grateful to a number of people who have influenced me and this dissertation.

My wife, Dr. Katrina Thomas, has shown a lot of support, as well as giving me a train to work on twice a week for three years.

I am indebted to my parents, Jack and Sue Schoonover, for all the love and support they have shown over the past 28 years, especially during my time in graduate school. They always encouraged my pursuit of knowledge and poverty.

My brother Brett and my sister Casey have always kept me grounded.

Dr. J.C. Gumbart, Matt Stiles, Beau Meredith, Dr. Adam Zysk, Marty Cantzler, and Grant Farrand have all been good friends and provided support and distractions, and the knowledge of when each was required.

The Wii night guys - Dom, J.D., and Paul - provided endless amusement in my final year of grad school.

Deborah Tedrick and Anja Visser have never minded when I show up at their place or drag their husbands away from home.

Prof. Taco Visser has been an excellent step-advisor, helping round me out as a scholar and academic.

The U.S. Fulbright Program allowed my work with Prof. Visser to begin, and for that I will always be thankful.

Prof. Randy Bartels at Colorado State University has supplied invaluable knowledge with regard to experimental data and the state of the art in fast pulse generation, and he has made numerous comments that have made this dissertation better.

Dr. Roberto Lavarello was instrumental in obtaining the data for the acoustic experiment.

The members of my preliminary and doctoral committees—Profs. Coleman, Eden, Oelze and Popescu—deserve special thanks for their helpful comments and time.

Dr. Bryn Davis has provided help, information, and beer in times of need.

Prof. Scott Carney has been my guide and mentor for these past five years. He has been a fount of knowledge, advice, and scotch for many of my troubles, both academic and personal. I will remain eternally grateful for all of his help.

TABLE OF CONTENTS

CHAPTER 1

INTRODUCTION

In which a problem is identified, and the beginnings of a solution are proposed

---

In recent years, the technology of fast pulses has advanced to a state such that the standard measurement theory for optical fields (stationary statistical optics) is no longer adequate to describe and predict the observed phenomena. Advances in nonlinear optical techniques have provided a means to generate and measure ultrafast pulses through methods such as FROG or SPIDER [1].

Statistical optics, or coherence theory [2, 3], is a measurement theory for nondeterministic light. Until recently, almost all optical experiments could be well modeled within the framework of the theory of stationary, random processes (or wide-sense stationary processes if only second order statistics, such as field intensity, are of interest). It is desirable to work within such a framework as the time-invariant nature of the statistics allows the use of powerful mathematical tools. For example, ergodicity and the Wiener-Khintchine-Einstein theorem [4, 5, 6] allow the meaningful interpretation of long-time-average and spectral measurements. However, the time-invariant nature of stationary fields limits the number of experiments that can be described by stationary statistics.

As an example, Magyar and Mandel showed that when a fast-gating system is used to invalidate the usual ergodicity assumption, structure resembling interference fringes in the overlap of fields generated by independent masers may be observed, contrary to what one would expect from slow detection systems [7]. More recently, fast pulse generation has

become the norm with pulse generation and detection being realized at the picosecond scale and faster [1].

Since many optical experiments are performed with short pulses, stationarity cannot be used in modeling the temporal characteristics of the optical field. Stochastic analysis is not constrained to only stationary random processes, however. Other types of random processes have been identified that share certain properties with stationary random processes. Some of these—intrinsically stationary processes, asymptotically stationary processes, cyclostationary processes and locally stationary processes [8]—allow for the analysis of signals that are not strictly time-invariant, and have relaxed this restrictions in some way. While optical models may be constructed around any of these classes of random processes, it is the purpose of this thesis to model the fields resulting from fast-pulse devices within the context of cyclostationary random processes. Within the theory of stationary random fields, an assumption of ergodicity provides an equivalence between time and ensemble averages. Thus the long-time integration performed by measurement devices (detectors) may be taken to be equivalent to an average of measurements over an ensemble of random fields. This allows for the construction of such ensembles including the construction of monochromatic realizations and the so-called generalized Fourier transform of the time-domain random process (which otherwise has no Fourier transform). The generalized Fourier transform and the interpretation of the cross-spectral density as a correlation function itself is crucial to much of the analysis of problems in spectroscopy and various spectral phenomena. Within the theory of cyclostationary processes, an analog of ergodicity may be found and is called cycloergodicity. An assumption of cycloergodicity allows time-averaged measurements of cyclostationary fields to be related to ensemble averages. Thus, a cyclostationary, cycloergodic model for optical fields provides many of the same insights as the stationary theory while encompassing a broader class of phenomena.

Up until now, optical pulse trains have been modeled deterministically. Within this model, an idealized optical pulse train consists of an infinite set of regularly spaced individual pulses. The spectrum for an idealized deterministic pulse train is given by the squared modulus of the Fourier transform of the field and consists of a spectral envelope,

associated with a single pulse profile, modulated by a sum of delta functions regularly spaced with a period equal to the pulse repetition frequency, a so-called delta comb. Pulsed optical fields, such as those generated by mode-locked lasers, do not exist in this idealized limit and the relevant noise properties have been studied through measurements of the pulse energy on a photodiode [9, 10, 11, 12, 13]. Theoretical and experimental studies of photodiode radio-frequency signals produced by short laser pulses in the picosecond [14] and femtosecond regime [15, 16, 17, 18, 19] provide detailed information about stochastic pulse train perturbations, including timing jitter, amplitude perturbations, and pulse width fluctuations. More recently, the role of the carrier-envelope offset phase noise in spectral-comb line broadening with mode-locked few-cycle lasers has been recognized, characterized, and controlled [20, 21, 22, 23]. In many of these experiments, attempts have been made to measure the coherence properties of pulsed optical systems, including estimating coherence properties [24, 25], the degree of spatial coherence of a beam [26, 27], and the power spectrum [11, 12]. However, the interpretation of these results is either based on the theory of stationary random processes, or a completely general theory of nonstationary fields ([11] being an exception in which cyclostationarity is invoked).

The theoretical study of general nonstationary fields has been mostly applied to the study of spectral measurements [28, 29, 30]. The time-dependent physical spectrum [28] was defined on the basis of instantaneous measurements made by a photo-detector in conjunction with some sort of spectral filter. These results were aided by the assumption of locally stationary or intrinsically stationary fields. The general form of the cross-spectral density [29] and the spectral density [30] for nonstationary fields without any assumptions with regard to the type of field statistics has also been investigated. However, some sort of prior knowledge is necessary to make unambiguous estimates of the statistical properties of the field or source based on measured data.

The theoretical study of nonstationary statistical optics, applied to pulse trains, has seen a recent resurgence [31, 32, 33, 34]. In the model presented in these references, a restricted class of nonstationary fields is considered in which a stationary field is modulated in a deterministic fashion — that is, an intrinsically stationary model [35]. While this model does not encompass all pulsed optical phenomena, it is a good bridge between a general

theory of nonstationary light and standard coherence theory. A further step in connecting nonstationary phenomena seen in experiments to standard (stationary) coherence theory is the use of a cyclostationary field model. The theory of cyclostationary random fields has been applied to measurement theory and the interpretation of certain optical experiments, including FROG and SPIDER [36], the behavior of cyclostationary plane waves [37] and beams [38] in interferometric systems, and the behavior of spectral correlation functions upon propagation [39].

The remainder of this dissertation is organized as follows: in Chapter 2, a brief review of cyclostationary and stationary random processes is given; in Chapter 3, the diffraction of cyclostationary beams is investigated and discussed; in Chapter 4, the special case of cyclostationary plane waves is investigated; in Chapter 5, correlation-dependent, propagation-induced changes in the generalized spectra of cyclostationary fields are exhibited; in Chapter 6, the generalization is made to electromagnetic (vectorial) fields; and in Ch. 7, some concluding remarks and avenues of future work are laid out.

CHAPTER 2

STATIONARY AND CYCLOSTATIONARY RANDOM VARIABLES AND PROCESSES

In which random processes are categorized, and stationary and cyclostationary processes are exposited

---

In this chapter, stationary and cyclostationary random processes are reviewed. Both stationary and cyclostationary random processes provide a useful model for nondeterministic optical fields and sources. The concepts of ergodicity and cycloergodicity will be applied to relate time averages to ensemble averages. This chapter concludes with a delineation of regimes, based on certain temporal quantities, that are relevant to most optical experiments.

2.1 Stationarity

A random process, $x(t)$, is called stationary if the probability density function for all moments of the random process remain invariant with respect to any shift in the time variable, t [8]. A slightly less restrictive class of random processes are the wide-sense stationary (WSS) processes. For wide-sense stationary processes, the statistics only to second order need to be invariant with respect to time shifts, *i.e.* $\langle x^*(t_1)x(t_2)\rangle = \langle x^*(t_1+\tau)x(t_2+\tau)\rangle$ for any time shift, τ, where $\langle\cdot\rangle$ denotes an ensemble average. The shift invariance implies that the autocorrelation of the function x is dependent only on the time difference, $t_2 - t_1$, *viz.* $\bar{\Gamma}_x(t_2 - t_1) = \langle x^*(t_1)x(t_2)\rangle$, where the overbar signifies that the correlation function is of a stationary random process.

Stationary random processes are, because of their time-invariant nature, not square

integrable, and thus only have a Fourier transform in the generalized sense. However, the Fourier transform of the two-time autocorrelation is a well-defined quantity:

$$\iint \mathrm{d}t_1\, \mathrm{d}t_2\, \bar{\Gamma}(t_2 - t_1) e^{i(\omega_2 t_2 - \omega_1 t_1)} = S(\omega_2)\delta(\omega_2 - \omega_1), \tag{2.1}$$

where the spectral density, $S(\omega)$, is the Fourier transform of $\bar{\Gamma}(\tau)$. This relationship, known as the Wiener-Khintchine-Einstein theorem [4, 5, 6], implies that the energy density of the random process at any frequency is found by evaluating the Fourier transform of the autocorrelation, and that the field is uncorrelated for any two distinct frequencies.

Up until now, all of the averages mentioned in this chapter have been ensemble averages, *i.e.* averages that take the form

$$\langle x^*(t_1)x(t_2)\rangle = \sum_\alpha p_\alpha\, {}^\alpha x^*(t_1)\, {}^\alpha x(t_2), \tag{2.2}$$

where p_α is the probability of the state α, and ${}^\alpha x(t)$ is the α^{th} member of the ensemble. In practice, the number of members in the ensemble can be quite large, and there is no practical way to find them from experiment. Rather, it is often assumed that the random processes are ergodic. For WSS random processes, an ergodic processes is one in which the time-average converges to the ensemble average [8]. In this way, the ensemble averages above and throughout this thesis may be related to measurements made in experiments by averaging the acquired signal in time. For example, if a stochastic signal $y(t) = x(t) + x(t-\tau)$ for some delay, τ, then the autocorrelation of y is given by

$$\Gamma_y(\tau) = 2\Gamma_x(0) + \Gamma_x(\tau) + \Gamma_x(-\tau). \tag{2.3}$$

For an ergodic signal, Γ_y is also the time-averaged intensity of the signal y, *i.e.*

$$\Gamma_y(\tau) = \int_{-T/2}^{T/2} \mathrm{d}t\, |y(t)|^2. \tag{2.4}$$

This relationship is only strictly true in the limit $T \to \infty$, but Eq. (2.4) is often a good approximation for values of T that are much larger than any relevant time scale in the

system being considered.

A collection of random processes, $\{x_n(t)\}$, are considered jointly stationary (at least in the wide sense), if for any two WSS random processes, the cross-correlation between those processes is also only a function of the time difference: $\bar{\Gamma}_{ij}(t_2 - t_1) = \langle x_n^*(t_1) x_j(t_2) \rangle$ for all x_i and x_j. Optical sources are often modeled as a collection of jointly stationary, WSS random processes. At the most fundamental level, optical fields are emitted by a collection of atoms. Depending on the state of the matter and the reason for emission (stimulated emission, spontaneous emission, thermal emission, etc.), the emitted field at each site, say, $x_n(t)$, will have varying degrees of statistical similarity to the field emitted at another site in the source, say $x_m(t)$, where it is assumed that there are a discrete number of emitters. In many cases of practical importance, the number of emitters is quite large, and the emitters are often close together, often well within a wavelength of the emitted light. In these cases, it is more practical to replace the collection of cross-correlations with a continuum:

$$x_i(t) \to Q(\mathbf{r}, t), \tag{2.5}$$

$$\bar{\Gamma}_{ij}(\tau) \to \bar{\Gamma}(\mathbf{r}_1, \mathbf{r}_2, \tau), \tag{2.6}$$

where $\mathbf{r}_i$ denotes the position within the optical source and τ is the time difference between the fields at the source at $\mathbf{r}_2$ and $\mathbf{r}_1$. $\bar{\Gamma}$ now represents the correlation of a continuous source, $Q(\mathbf{r}, t)$, with itself, but at two points and two times. The two-point, two-time correlation function is known as the mutual coherence function of the source. The mutual coherence function for the field propagated from a stationary optical source is derived in Appendix A.

2.2 Cyclostationarity

Cyclostationary random processes are a less restrictive class of random processes than stationary random processes. A random process is cyclostationary (at least in the wide-sense) if the statistics, up to second order, are invariant with respect to the time shift

$t \to t + T_0$ for some specific T_0 [8, 40]. Thus, the correlation function for a cyclostationary random process $x_c(t)$ obeys the relationship

$$\Gamma_x(t_1, t_2) = \Gamma_x(t_1 + T_0, t_2 + T_0), \tag{2.7}$$

where $\Gamma_x(t_1, t_2) = \langle x_c^*(t_1) x_c(t_2) \rangle$. The periodicity of the correlation function, as seen in Eq. (2.7), allows for a Fourier series representation of the correlation function, with fundamental frequency $\omega_0 = 2\pi/T_0$, *e.g.*

$$\Gamma_x(t - \tau, t) = \sum_{n=-\infty}^{\infty} C_n(\tau) e^{-in\omega_0 t}, \tag{2.8}$$

where the C_n are a collection of generalized correlation functions, each of which is a function only of the time difference, τ.

As with stationary random processes, the two-time Fourier transform of the autocorrelation of a cyclostationary random process can be found. In this case, one finds that

$$\Gamma_x(t - \tau, t) = \sum_n C_n(\tau) e^{-in\omega_0 t} \leftrightarrow W_x(\omega, \omega + \Omega) = \sum_n \tilde{C}_n(\omega) \delta(\Omega - n\omega_0), \tag{2.9}$$

where $\tilde{C}_n(\omega)$ is the Fourier transform of $C_n(\tau)$. Equation (2.9) is a generalization of the Wiener–Khintchine–Einstein (WKE) theorem as may be seen by taking the $T_0 \to \infty$ ($\omega_0 \to 0$) limit. In the usual form of the WKE theorem, the delta function $\delta(\Omega)$ indicates that the field is uncorrelated across frequencies. In this generalized form, it is clear that the field is correlated only at discretely spaced frequencies.

Analogously to a stationary random process, a collection of cyclostationary random processes, $\{x_n\}$, are called jointly cyclostationary if each random process is cyclostationary with period T_0, and the cross-correlation functions are also periodic with the same period, T_0. In the same manner as in the case of stationary sources in the previous section, a

cyclostationary optical source can be written as a function of two position variables:

$$\langle Q^*(\mathbf{r}_1, t-\tau)Q(\mathbf{r}_2, t)\rangle = \Gamma_Q(\mathbf{r}_1, \mathbf{r}_2, t-\tau, t) = \sum_n Q_n(\mathbf{r}_1, \mathbf{r}_2, \tau)e^{-in\omega_0 t}. \tag{2.10}$$

The Q_n are generalized mutual coherence functions. The mutual coherence function for the cyclostationary source likewise has a Fourier representation

$$\Gamma_Q(\mathbf{r}_1, \mathbf{r}_2, t-\tau, t) = \sum_n Q_n(\mathbf{r}_1, \mathbf{r}_2, \tau)e^{-in\omega_0 t}, \tag{2.11}$$

$$W_Q(\mathbf{r}_1, \mathbf{r}_2, \omega, \omega+\Omega) = \sum_n \tilde{Q}_n(\mathbf{r}_1, \mathbf{r}_2, \omega)\delta(\Omega - n\omega_0). \tag{2.12}$$

The $\tilde{Q}_n(\mathbf{r}, \mathbf{r}, \omega)$ are generalized spectra and the $\tilde{Q}_n(\mathbf{r}_1, \mathbf{r}_2, \omega)$ are generalized cross-spectra. In Appendix A, a propagation law for the generalized cross-spectra is derived.

2.2.1 Intrinsically Stationary, Cyclostationary Optical Model

In this dissertation, a specific type of cyclostationary optical field is considered, namely one in which a stationary optical field is modulated in time by a periodic function, *i.e.*

$$\Gamma(\mathbf{r}_1, \mathbf{r}_2, t_1, t_2) = \bar{\Gamma}(\mathbf{r}_1, \mathbf{r}_2, t_2 - t_1)h^*(t_1)h(t_2), \tag{2.13}$$

where $h(t)$ is the periodic function. As long as $h(t)$ is periodic, Γ is cyclostationary, with the same period as $h(t)$. The function $h(t)$ has two representations that are particularly useful:

$$h(t) = \sum_n h_p(t - nT_0) \tag{2.14}$$

$$= \sum_n h_n e^{-in\omega_0 t}. \tag{2.15}$$

While both models are formally the same, the first, Eq. (2.14), is suggestive of a pulse train, where $h_p(t)$ describes the shape of the pulse, including pulse duration, duty cycle, chirp, and other temporal effects. Both representations will be used throughout this

dissertation. Here, $h(t)$ is called a shutter function.

Since the underlying source is assumed to be stationary, the cross-spectal density, W, for a field with mutual coherence function of the form of Eq. (2.13) takes the form

$$\begin{aligned} W(\mathbf{r}_1, \mathbf{r}_2, \omega, \omega + \Omega) &= \iint \mathrm{d}t \, \mathrm{d}\tau \, \Gamma(\mathbf{r}_1, \mathbf{r}_2, t - \tau, t) e^{i(\omega\tau + \Omega t)} \\ &= \sum_{m,n} h_n^* h_{m+n} \bar{W}(\mathbf{r}_1, \mathbf{r}_2, \omega - \omega_0 n) \delta(\Omega - m\omega_0), \end{aligned} \tag{2.16}$$

where, again, the bar denotes the cross-spectral density of the underlying stationary source.

The intrinsically stationary, cyclostationary model encompasses only a small subset of possible cyclostationary fields, but may well-model the field for certain methods of short pulse generation. For example, in high harmonic generation, a laser pulse is incident on an atomic gas, which then emits at harmonics of the impinging laser frequency. The collection of atoms serve as the stochastic source, and the impinging laser field acts as a kind of modulation. Likewise, optical pulses produced by Q-switching [41] may be considered cyclostationary when the modulation of the loss in the cavity is periodic.

2.2.2 Temporal Regimes for Cyclostationary Fields

The model presented in this dissertation represents a stochastic pulsed field as a modulated stationary optical field. The underlying stochastic field is assumed to have a coherence time τ_c, the duration of the single pulse $h_p(t)$ is characterized by T and the pulses are repeated with a period T_0. The relationship between these three time scales (T_0, T, and τ_c) determines the statistical properties of the pulsed field. Pulsed fields can be readily classified into several distinct regimes based on these parameters. Three of these regimes cover most physically realizable experiments.

- Regime I is defined by $T < T_0 < \tau_c$. In this regime pulses separated by several T_0 exhibit significant correlations. This regime includes devices such as stable mode-locked pulses with long-term fluctuations in the pulse properties, which may include timing jitter, amplitude fluctuations, carrier-envelope phase fluctuations, etc. In this regime non-deterministic behavior results in a modest broadening of spectral

comb lines [9]. In terms of Eq. (2.16), the width of $\bar{W}(\mathbf{r}_1, \mathbf{r}_2, \omega)$ is less than the comb spacing $2\pi/T_0$, so the comb structure remains, albeit with a broader line width.

- Regime II is defined by $T < \tau_c < T_0$, where pulses separated by the pulse period T_0 may exhibit a significant statistical relationship, but pulses separated by multiple repetition periods are statistically uncorrelated. Highly unstable mode-locked lasers may operate in this regime. Here one expects the power spectral density to be continuous as the spectral width of the underlying stationary field approaches the repetition frequency $\omega_0 = 2\pi/T_0$ of the pulsed light field. However, the bandwidth of the signal is still determined by the pulse duration T.

- Regime III is defined by $\tau_c \ll T < T_0$, the so-called continuous-wave limit [42]. In this regime, the pulses are separated by significantly more than τ_c and so the fields in separate pulses are not statistically related. Additionally, the condition $\tau_c \ll T$ indicates that the field at the beginning of a pulse is statistically uncorrelated with the field at the end of the pulse. The power spectral density in this regime is dominated by that of the underlying stochastic field. The convolution with $\bar{W}(\mathbf{r}_1, \mathbf{r}_2, \omega)$ in Eq. (2.16) destroys the comb structure and spreads the spectrum beyond the limits of the deterministic pulse.

CHAPTER 3

DIFFRACTION AND INTERFEROMETRY FOR CYCLOSTATIONARY FIELDS

In which a cyclostationary beam illuminates an interferometer

---

In this chapter, the propagation of cyclostationary fields is examined. Specifically, an intrinsically stationary, cyclostationary beam model is used to elucidate certain properties of fields propagated from cyclostationary sources. Interferometry, as it is used for stationary fields, is described in Section 3.1. Simulations of cyclostationary fields are examined in the context of interferometry in Section 3.2. These simulations include interferometric measurements made in the near, intermediate (Fresnel) and far zones from the source. Potential uses of these interferometric techniques in elucidating statistical properties of the original source and problems with setting these measurements in the stationary theory are discussed. New phenomena not seen in either the stationary case or the deterministic case are predicted.[1]

3.1 Interferometry

The propagation laws for cyclostationary fields are derived in Appendix A. One can use these results to find the second-order statistics of the field propagated from a known statistical source. However, one often does not have all of the information about the source necessary to properly determine the propagated field. Rather, one makes measurements of the field intensities in a device such as an interferometer to ascertain the coherence

[1]This chapter is based on R.W. Schoonover, B.J. Davis, R.A. Bartels, and P.S. Carney, "Propagation of spatial coherence in fast pulses," *J. Opt. Soc. Am. A* **26**, 1945–1953 (2009).

properties of the field, and then make inferences about the coherence properties of the source.

The field, or moments and correlations of the field, may be measured with some form of interferometry. Young's classic interference experiment [43] is used to measure two-point correlations of optical fields. The original experiment, performed by Thomas Young in 1801, was performed to test the wave theory of light. Many other properties of optical fields have been ascertained from a two-slit or two-pinhole experiment [44, see Chap. 15 and references therein].

The utility of a Young's interferometer springs from the fact that, for stationary fields, the visibility of the interferogram is equal to the magnitude of the spatial degree of coherence of the field at the two apertures. The interferogram produced in Young's style of experiment also can be used to determine the approximate coherence time (and thus the bandwidth) of the impinging field. The extent to which spatial correlation properties of the field or the source that generated the field may be investigated through interferometric measurements has not been elsewhere established and is addressed below.

The Young's two-pinhole interferometer, as shown in Fig. 3.1, contains a screen $\mathcal{A}$ that includes two pinhole apertures and a detector in the plane $\mathcal{D}$, parallel to $\mathcal{A}$. The screen $\mathcal{A}$ is chosen to be parallel to the source plane, here defined by the shutter, and is a distance z' away from the source.

For points P on the detection screen, the ensemble average of the instantaneous intensity as a function of time is related to the fields in the two pinholes by the equation

$$\begin{aligned}
\Gamma_{\mathcal{D}}(P,P,t,t) &= |K_1|^2\Gamma_{\mathcal{A}}(Q_1,Q_1,t-R_1/c,t-R_1/c) \\
&+ |K_2|^2\Gamma_{\mathcal{A}}(Q_2,Q_2,t-R_2/c,t-R_2/c) \\
&+ K_1^*K_2\Gamma_{\mathcal{A}}(Q_1,Q_2,t-R_1/c,t-R_2/c) \\
&+ K_1K_2^*\Gamma_{\mathcal{A}}(Q_2,Q_1,t-R_2/c,t-R_1/c), \qquad (3.1)
\end{aligned}$$

where $\Gamma_{\mathcal{A}}$ is the mutual coherence function at plane $\mathcal{A}$, the K_i are constant (for observation points close to the optical axis) factors that depend on the area of the holes and the

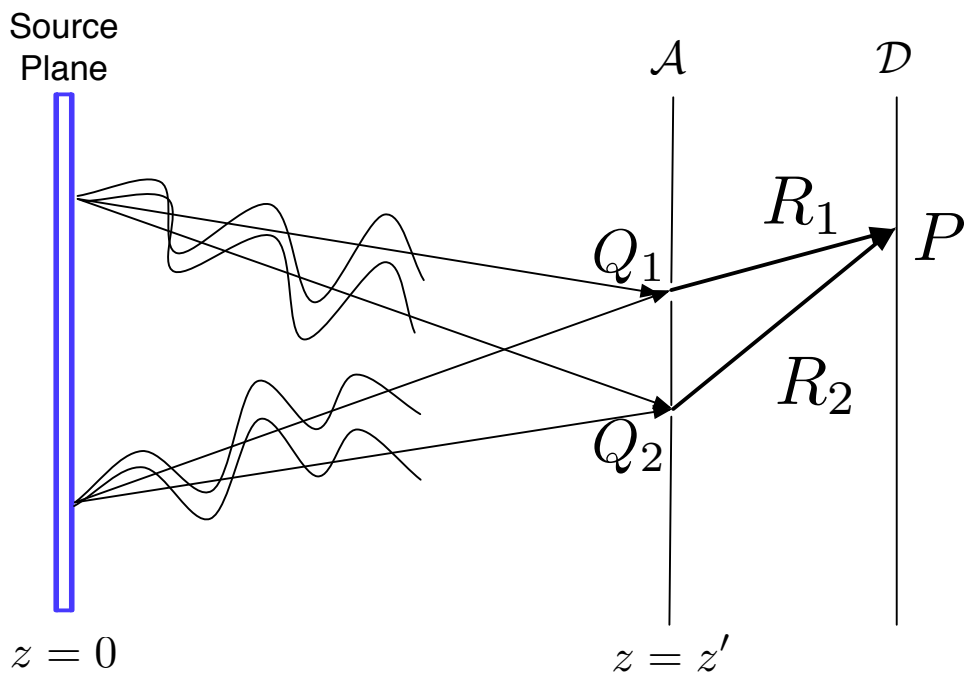

Figure 3.1: A diagrammatic sketch of the source and interferometer. The field radiated by two points in the source plane are shown propagating to the interferometer screen.

distance R_i from the i^{th} pinhole to the point P (see Fig. 3.1). For fields that are quasi-monochromatic, $K_i = -i\mathrm{d}\mathcal{A}/\bar{\lambda}R_i$ [45], where $\bar{\lambda} = 2\pi c/\omega_c$ and $\mathrm{d}\mathcal{A}$ is the area of the pinhole. Using Eq. (3.1), the interferogram created by a field with a known cross-spectral density at the pinholes may be computed.

The visibility in an interferometric measurement [2] is

$$\mathcal{V} = \frac{I_{\max} - I_{\min}}{I_{\max} + I_{\min}}. \tag{3.2}$$

For stationary fields, when the intensity in each pinhole is approximately the same, the visibility is related to the complex degree of coherence, γ, via $\mathcal{V} = |\gamma[Q_1, Q_2, (R_2 - R_1)/c]|$, where $\gamma(Q_1, Q_2, \tau) = \Gamma(Q_1, Q_2, \tau)/\sqrt{\Gamma(Q_1, Q_1, 0)\Gamma(Q_2, Q_2, 0)}$ is a normalized measure of statistical similarity of the field at two points. The visibility ranges from zero to unity as the field goes from incoherent to fully coherent.

3.2 Simulations

In order to illustrate the observable effects of cyclostationarity and their connection to the parameters of the source in pulsed, spatially partially coherent fields, numerical simulations were performed. Closely following the method outlined in [46], realizations of a discrete random process were generated to model the stationary source, assumed to be planar. For all of the simulations in this manuscript, the modulation function was taken to be a square wave with duration T and duty cycle T/T_0. The correlation function of the field at the shutter was taken to be factorizable in time and space, *viz.*,

$$\bar{\Gamma}(\mathbf{r}_1, \mathbf{r}_2, \tau) = \Gamma'(\tau) F(\mathbf{r}_1, \mathbf{r}_2), \tag{3.3}$$

where F is a function of the two position coordinates $\mathbf{r}_1$ and $\mathbf{r}_2$ that lie in the shutter plane, and expresses the spatial correlations of the source and the amplitudes across the source plane. For the simulations, $\bar{\Gamma}$ and F were taken to be Gaussian:

$$\Gamma'(\tau) = \exp(-\tau^2/2\tau_c^2) \exp(-i\omega_c \tau), \tag{3.4}$$

$$F(\mathbf{r}_1, \mathbf{r}_2) = \exp(-r_1^2/4\sigma_s^2) \exp(-r_2^2/4\sigma_s^2) \exp(-|\mathbf{r}_1 - \mathbf{r}_2|^2/2\sigma_g^2), \tag{3.5}$$

where σ_s and σ_g are the beam width and coherence length at the secondary source, respectively, ω_c is the central frequency, and τ_c is the coherence time. For all simulations, except where noted, the central frequency is $\omega_c = 1 \times 10^{15}$ rad/s ($\lambda_c = 1.88\,\mu$m), the interferometer has pinhole separation $s = 2$ mm and the distance between the screen and the detection plane is $d = 50$ mm. The beam width and coherence lengths were chosen throughout this paper to ensure that the resultant field is always beam-like, that is, both of the length parameters are much larger than the largest wavelength for which the cross-spectral density is not negligible. The source plane was discretized, and an independent zero-mean, complex Gaussian process was generated for each point for each time step in the simulation. A two-dimensional spatial filter was applied to the complex Gaussian process for each time step to give the chosen spatial coherence properties, while a one-dimensional temporal filter was applied at each position in the discretized source to

give the chosen temporal coherence properties. The random process at each point source was then weighted to give the chosen field amplitude. The coherence properties and amplitude used in these simulations are defined in Eqs. (3.3)-(3.5).

Following the simulation of the source in the plane, the temporal modulation, defined by h, was applied to the source, and the field was propagated using the causal Green function [see Eq. (A.6)], treating each point in the plane as a primary point source. The total field at each pinhole was calculated by summing the contributions from each source point. It was assumed that the detector was frequency-independent, *i.e.* that the measured intensity in the detection plane was the square magnitude of the sum of the two incident fields. Long time averages were taken of the instantaneous intensity in the detection plane and plotted for a variety of source distributions.

Simulations were run for sources in the different temporal regimes described above with different spatial coherence and intensity profiles. The resultant fields generated by such sources were then propagated numerically using Eq. (A.6) to the two pinholes, and the resultant interferograms were calculated. In these simulations, a Young's interferometer (*i.e.* a planar screen with two pinholes, $\mathcal{A}$, and a detection plane, $\mathcal{D}$, as seen in Fig. 3.1) was placed at three different distances from the source - one near to the source, one in an intermediate (Fresnel) zone, and one in the far zone - to help discern different propagation effects.

In Figs. 3.2-3.7, 18 interferograms are shown for a source characterized by three time scales (the pulse duration, T; the repetition period, T_0; and the coherence time, τ_c), two sets of spatial parameters (the coherence length, σ_g; and the beam width in the plane, σ_s), and in three separate detection regions (zones). A change in zone denotes a change in the distance between the shutter and the plane $\mathcal{A}$ in Fig. 3.1. It may be noted that as the spatial coherence of the source is increased, the visibility of the fringes increases as measured in both the Fresnel and near zones. In the far zone, the interferograms appear to have unit visibility, regardless of the spatial coherence properties of the source.

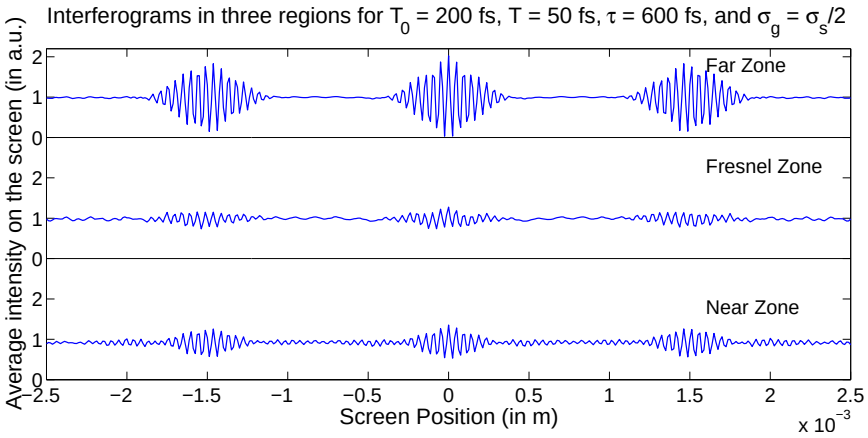

Figure 3.2: Simulated interferograms for a source with $T_0 = 200$ fs, $T = 50$ fs, $\tau_c = 600$ fs, and $\sigma_g = \sigma_s/2 = 1$ mm. The top panel contains the interferogram as would be measured in the far zone (100 m away from the source), the middle panel contains the interferogram as would be measured in the Fresnel zone (500 mm away from the source), and the bottom panel contains the interferogram as would be measured in the near zone (2 mm away from the source). This source is in Regime I.

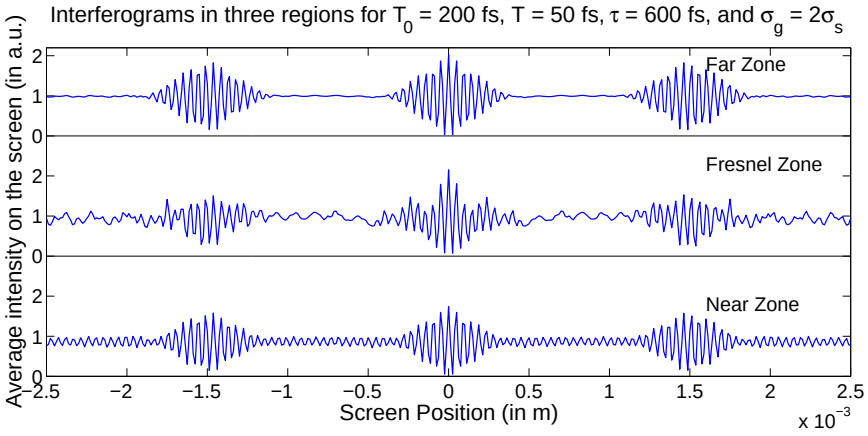

Figure 3.3: Simulated interferograms for a source with $T_0 = 200$ fs, $T = 50$ fs, $\tau_c = 600$ fs, and $\sigma_g = 2\sigma_s = 4$ mm. The top panel contains the interferogram as would be measured in the far zone (100 m away from the source), the middle panel contains the interferogram as would be measured in the Fresnel zone (500 mm away from the source), and the bottom panel contains the interferogram as would be measured in the near zone (2 mm away from the source). This source is in Regime I.

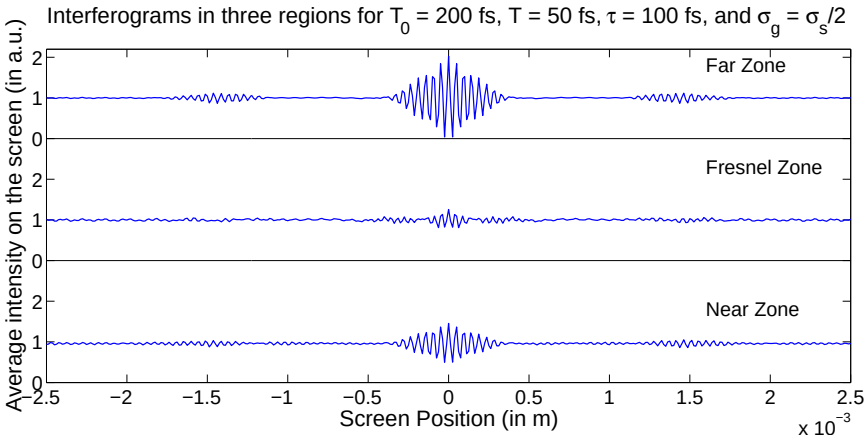

Figure 3.4: Simulated interferograms for a source with $T_0 = 200$ fs, $T = 50$ fs, $\tau_c = 200$ fs, and $\sigma_g = \sigma_s/2 = 1$ mm. The top panel contains the interferogram as would be measured in the far zone (100 m away from the source), the middle panel contains the interferogram as would be measured in the Fresnel zone (500 mm away from the source), and the bottom panel contains the interferogram as would be measured in the near zone (2 mm away from the source). This source is in Regime II.

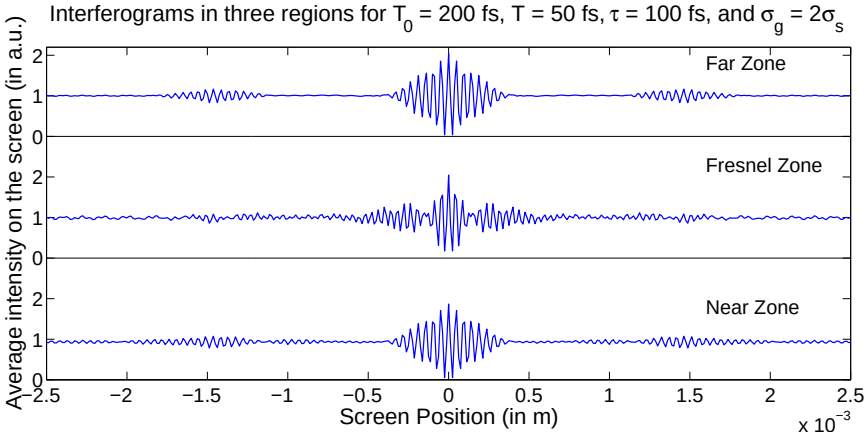

Figure 3.5: Simulated interferograms for a source with $T_0 = 200$ fs, $T = 50$ fs, $\tau_c = 200$ fs, and $\sigma_g = 2\sigma_s = 4$ mm. The top panel contains the interferogram as would be measured in the far zone (100 m away from the source), the middle panel contains the interferogram as would be measured in the Fresnel zone (500 mm away from the source), and the bottom panel contains the interferogram as would be measured in the near zone (2 mm away from the source). This source is consistent with being in Regime II.

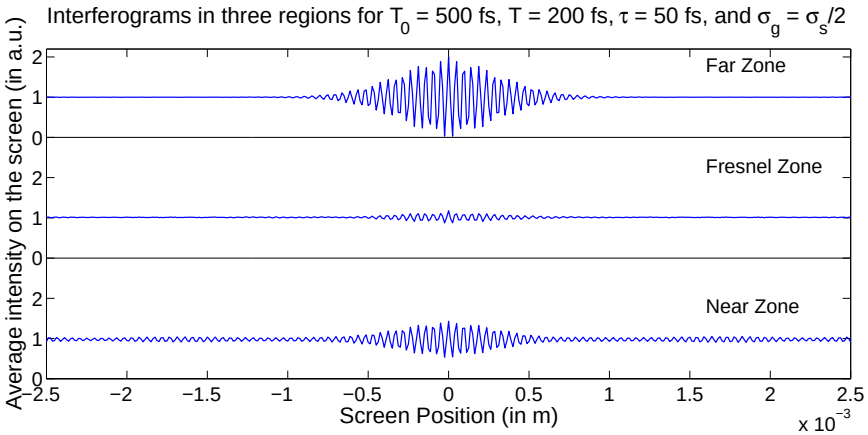

Figure 3.6: Simulated interferograms for a source with $T_0 = 500$ fs, $T = 200$ fs, $\tau_c = 50$ fs, and $\sigma_g = \sigma_s/2 = 1$ mm. The top panel contains the interferogram as would be measured in the far zone (100 m away from the source), the middle panel contains the interferogram as would be measured in the Fresnel zone (500 mm away from the source), and the bottom panel contains the interferogram as would be measured in the near zone (2 mm away from the source). This source is in Regime III.

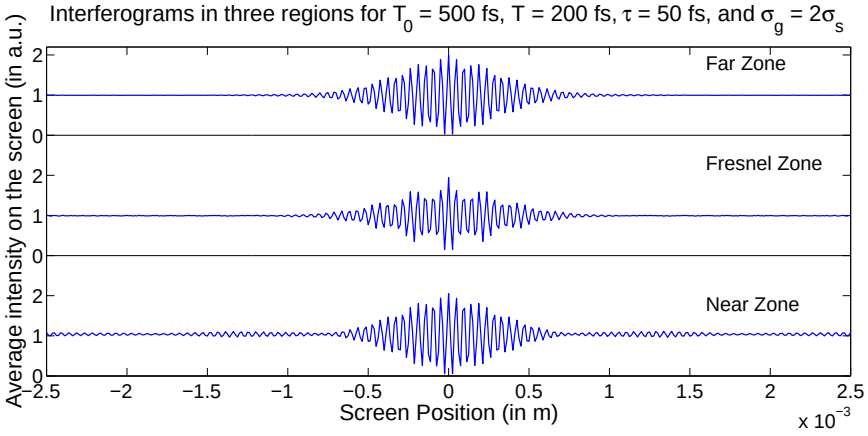

Figure 3.7: Simulated interferograms for a source with $T_0 = 500$ fs, $T = 200$ fs, $\tau_c = 50$ fs, and $\sigma_g = 2\sigma_s = 4$ mm. The top panel contains the interferogram as would be measured in the far zone (100 m away from the source), the middle panel contains the interferogram as would be measured in the Fresnel zone (500 mm away from the source), and the bottom panel contains the interferogram as would be measured in the near zone (2 mm away from the source). This source is in Regime III.

Far zone

Much as in the theory of stationary fields, the cross-spectral density in the far zone is related to the Fourier transform of the source cross-spectral density function F [see Eq. (A.21)]. This relationship obtains when the source is far from the observation point(s) and thus the spectral Green function in Eq. (A.12) can be replaced by $\tilde{G}(\mathbf{r}, \mathbf{r}'; k) \approx \exp(ikr)\exp(-ik\hat{r} \cdot \mathbf{r}')/r$. For the specific geometry described in this paper, the field incident on the two pinholes in the far zone is indistinguishable from a single polychromatic plane wave traveling in the $\hat{z}$ direction with cross-spectral density

$$W^{(\infty)}(\omega, \omega + \Omega) = \tilde{F}(\mathbf{0}, \mathbf{0}) A(\omega, \omega + \Omega) e^{i\Omega r}/r^2, \tag{3.6}$$

where $\tilde{F}$ is the four-dimensional Fourier transform of F, $A(\omega, \omega + \Omega)$ is the two-frequency cross-spectral density of the modulated source,

$$A(\omega, \omega + \Omega) = \sum_{m,n} h_n^* h_{m+n} \bar{W}(\omega - \omega_0 n) \delta(\Omega - m\omega_0), \tag{3.7}$$

and $W^{(\infty)}$ is position-independent for small pinhole spacings, s. Thus, for sources that are well described by Eq. (3.3), only the temporal correlation and modulations, described by the function A, may be investigated. The spatial correlations of the source are manifest only in the constant multiplier $\tilde{F}(\mathbf{0}, \mathbf{0})$. The minor variations from unity are a result of the very minor variations of the angular positions of the two pinholes viewed from the source plane. A more detailed analysis of interferometric measurements of cyclostationary plane waves can be found in Chapter 4.

Fresnel zone

The Fresnel zone is an intermediate region away from the source and near the beam axis. In this region, the spectral Green function, Eq. (A.12), takes the form $\tilde{G}(\mathbf{r}, \mathbf{r}'; k) \approx \exp(ikz)/z \exp[ik(\boldsymbol{\rho} - \boldsymbol{\rho}')^2/(2z)]$. In this zone, the radiated field does not appear as a single polychromatic plane wave as in the far zone. The field radiated from different points

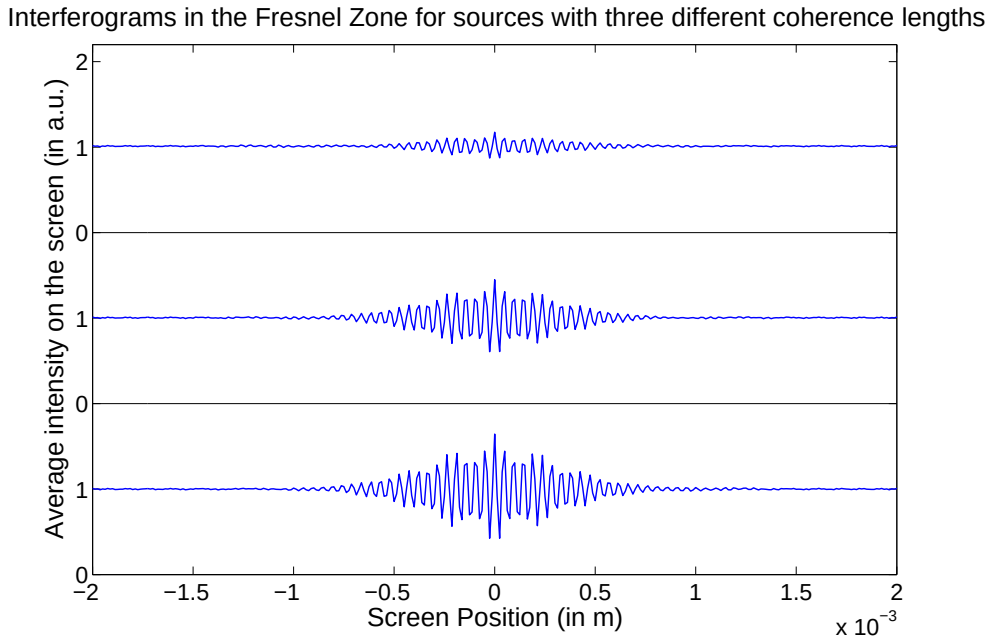

Figure 3.8: Simulated interferograms for three sources with $T_0 = 500$ fs, $T = 200$ fs, $\tau_c = 50$ fs and $\sigma_s = 2$ mm. In the top panel, the simulated source has coherence length $\sigma_g = 1$ mm; in the middle panel, the simulated source has coherence length $\sigma_g = 1.5$ mm; and in the bottom panel, the simulated source has coherence length $\sigma_g = 2$ mm.

in the source plane may have differences in time of flight to the pinholes of up to 15 fs for the parameters in these simulations. The field radiated from these points, though, are only partially correlated. Depending on the coherence length at the source, the contributions to the field at the pinholes from these points may, upon averaging, interfere, creating an interferogram that has a central peak wider than that found in the far zone. For example, in Fig. 3.5, the major peak in the interferogram as simulated in the Fresnel zone is wider than the peaks in the other two zones, whereas in Fig. 3.6, the interference effects essentially wash out all the fringes in the Fresnel zone interferogram. In Fig. 3.8, the Fresnel-zone interferograms for three sources with identical temporal properties but different spatial coherence lengths are displayed. As the coherence length at the source increases, the field at the two pinholes more closely resembles the field that would be produced by a fully spatially coherent source. Note that the central peak becomes wider and more visible as the coherence length at the source increases.

Near zone

In the near zone, both the amplitude rolloff of $1/r$ and the varying phase accumulations between all source points and the pinholes are important; thus, the propagator $\tilde{G}$ cannot be simplified. In Figs. 3.2-3.7, it is evident that the central peak has approximately the same width as in the far zone. This width is determined by the smaller of the pulse duration or coherence time. This is due to the fact that the interferometer is essentially sampling the field only at the points nearest the pinholes. The duration of the pulse in the pinholes is then essentially the same as at the source. This is in contrast to the Fresnel zone, where the duration of the pulse has increased because of the varying times of flight to the pinholes from the extended source. The visibility of the main interferogram is an increasing function of the spatial coherence length at the source.

In both the near and intermediate zones, the visibility of the center fringe increases as the spatial coherence of the source increases. The far zone visibility measurements are, to a good approximation, independent of the spatial correlation properties of the source. In the Fresnel zone geometry, the field in each pinhole is dependent on the fields over a significant area of the source. The varying times of flight across this area cause the observed data to exhibit a multiplex dependence on the spatial and temporal statistics of the source. For a stationary source, variation of the statistics is independent of the origin of time. The non-stationary nature of the sources considered complicates the interpretation of the Fresnel zone data, as the source statistics may change as a function of the times of flight. Measurements in the near zone, however, may be sufficient for determining spatial correlation properties of the source, as will be seen in the next section.

3.2.1 Determining Spatial Coherence Properties

It is clear from the previous section that no meaningful quantitative statements can be made about the spatial coherence properties of the source from measurements made in the far zone, and that measurements made in the Fresnel zone may only be useful for qualitative statements about the spatial partial coherence. However, when the interferometer is placed near the source (for beam-like fields, within approximately the

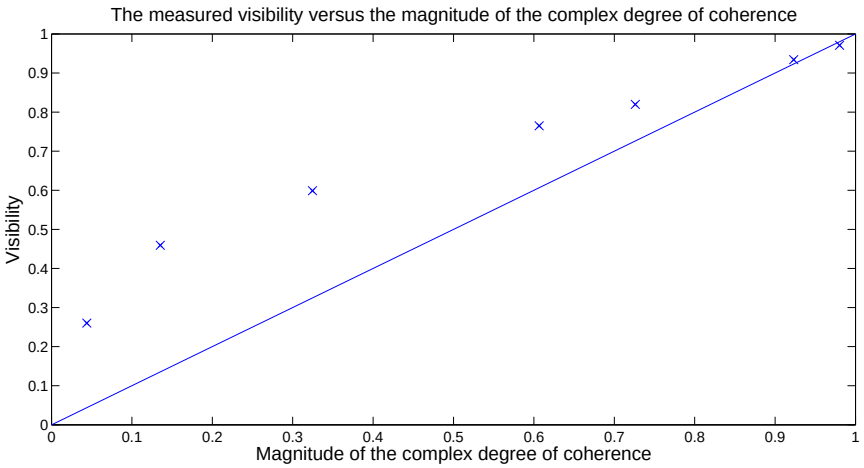

Figure 3.9: A plot of the visibility versus the magnitude of the complex degree of coherence for a source characterized by $T_0 = 200$ fs, $T = 50$ fs, $\tau_c = 100$ fs, $\sigma_s = 2$ mm and $\sigma_g = 1$ mm. The interferometer is simulated to be 2 mm away from the secondary source (one beam width). The straight line represents a perfect match between the simulated visibility and the calculated magnitude of the complex degree of coherence.

width of the intensity in the source plane), there is a relationship between the visibility in the interferograms and the complex degree of spatial coherence of the underlying stationary process when the stationary process is factorizable, as in Eq. (3.3).

In Fig. 3.9, the near zone visibility of the propagated field is plotted against the magnitude of the complex degree of coherence of the source between the two points nearest each pinhole. In the example considered here, $\gamma_{12}(\mathbf{r}_1, \mathbf{r}_2) = \exp(-|\mathbf{r}_1 - \mathbf{r}_2|^2/2\sigma_g^2) = \exp(-s^2/2\sigma_g^2)$. Simulations were run for varying pinhole spacings, s, and the measured visibility was plotted against γ_{12}. When the interferometer is close to the source, the measurements are in reasonable agreement. For pairs of points that are farther from the point of maximal intensity of the beam (points that result in fields that exhibit lower visibility), the approximation that the primary contribution to the field in the pinhole comes from the point in the source directly across from it becomes less valid. This is because the field amplitude at that point may be much smaller than at neighboring points. This explains why the visibility falls off more slowly in Fig. 3.9 than the magnitude of the complex degree of coherence of the field between the two points nearest the pinholes.

3.2.2 Single Shot Measurements

One of the most obvious ways in which the fields presented in this paper differ from the standard stationary theory is that there exists an "on" and "off" time for the radiated field. Depending on the repetition rate of the pulses and the type of detector used, this creates a window in which to collect measurements from each pulse individually. However, these single shot measurements of intensity [25, 27] are not necessarily indicative of the time-averaged intensity measurements as presented in previous sections. Only in certain limiting cases, such as when the pulse time is long compared to the coherence time and the coherence length is long compared to the beam width, might a single shot measurement be indicative of the time averaged behavior (*i.e.* the field is in Regime III). In Fig. 3.10, the interferograms generated by averaging over 800 pulses (of time T_0), are shown as would be measured in the Fresnel zone. Three single-shot measurements for the same system are shown in Fig. 3.11. Note that the single shot measurements of the intensity do not resemble the time-averaged intensity, even though the top panel of Fig. 3.11 does resemble a traditional interferogram. The width of the peak in the interferograms for the single shot measurements are indicative of the pulse time, T (an interferogram extending out to ± 1.5 mm corresponds to a pulse time of 200 fs for this geometry). The width of the peak in the time-averaged measurement, though, is indicative of the coherence time at the two pinholes (an interferogram extending out to ± 0.5 mm corresponds to an effective time of 66 fs for this geometry). Because of propagation effects, the coherence time of the field at the pinholes is not the coherence time of the field at the source.

Using a cyclostationary model, diffraction and interference effects have been illustrated for spatially partially coherent pulses. Standard interferometric techniques were used to simulate a wide variety of experiments with nonstationary fields. Some of these experiments have no analog in the analysis of stationary fields. For example, it was shown that single shot measurements of intensity in an interferometer are not necessarily indicative of time-averaged measurements, and thus single shot measurements cannot be used to infer coherence properties of the source. The interferometric data was also analyzed for different regions away from the source. The field in the far zone results from

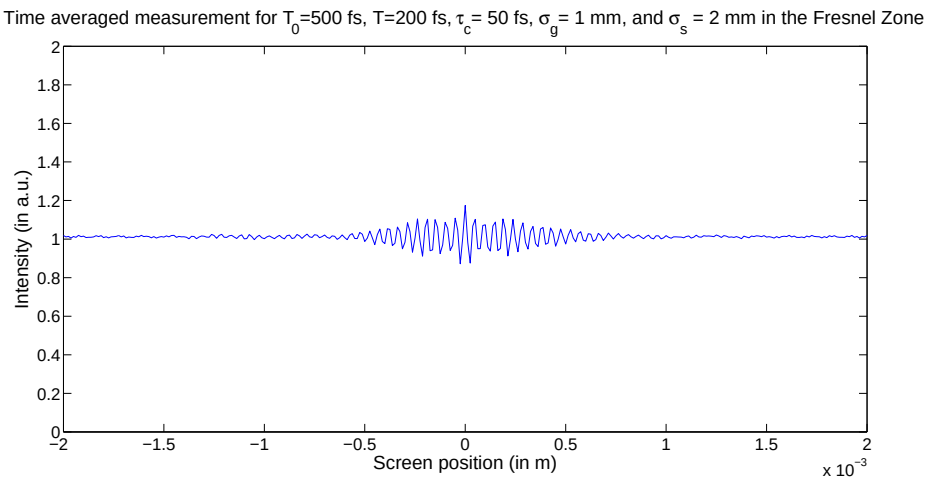

Figure 3.10: The results of a simulation of the time-averaged intensity (taken over 800 pulses) for a field parameterized by $T_0 = 500$ fs, $T = 200$ fs, $\tau_c = 50$ fs, $\sigma_s = 2$ mm and $\sigma_g = 1$ mm as would be measured in the Fresnel zone.

equally weighted contributions from all points in the source plane. The spatial coherence of the source thus only affects the coherence function in the far zone through a constant multiplier. In the Fresnel zone, the field results from unequally weighted contributions from multiple points in the source plane, with each contribution associated with a different propagation time. In stationary fields, the statistics are sensitive only to delay differences, whereas in the case considered here, there is a dependence on absolute time that complicates the results considerably. In the near zone, the Young's interferometer essentially samples the field at the source plane at points closest to the pinholes. As a result, the effects of partial spatial coherence of the source are manifest as a constant multiplier on the interference terms, and the temporal coherence determines unambiguously the shape of the interferogram. Based on this analysis, it was also shown that from measurements in the far zone, only temporal properties of the source can be inferred, and that the spatial coherence length of the source can be determined only from measurements in the near zone.

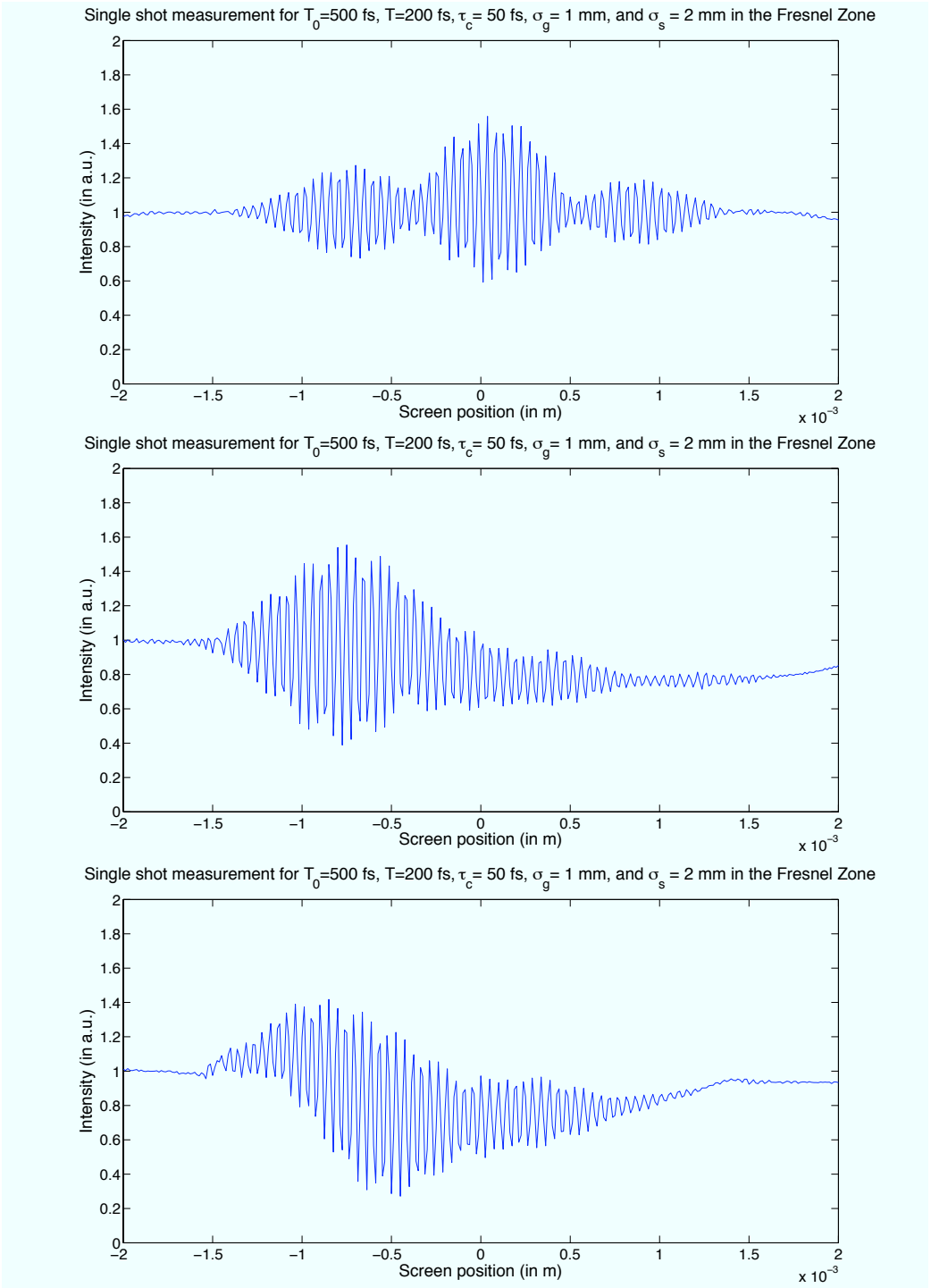

Figure 3.11: The results of three simulations of a single shot measurement for a field parameterized by $T_0 = 500$ fs, $T = 200$ fs, $\tau_c = 50$ fs, $\sigma_s = 2$ mm and $\sigma_g = 1$ mm as would be measured in the Fresnel zone.

CHAPTER 4

ANALYSIS OF CYCLOSTATIONARY PLANE WAVES IN INTERFEROMETRY

In which the reduction to plane wave illumination makes tractable the analytics

---

In this chapter, the results found for the far zone measurements as seen in Chapter 3 are expanded upon. The time-averaged intensity of a plane wave found at the detection plane of an interferometer (see Fig. 3.1) can be calculated analytically for certain models. It is shown that the interferograms created in such experiments are ambiguous as to the specific temporal properties of the incident field. In Section 4.1, the intrinsically stationary, cyclostationary model for optical fields is applied to plane wave fields. Analytic forms for the intensity in a Young's interferometer are found. The results are compared to simulations in Section 4.2.[1]

4.1 Interferometric Measurement

Like previous chapters, this chapter uses an intrinsically stationary, cyclostationary model in which a stationary, random process with cross-spectral density, $\bar{W}$, is modulated by a periodic function $h(t)$. In order for the resulting field to be a cyclostationary plane wave, the source must be a spatially homogeneous, planar source. The spectrum of the source is assumed to be Gaussian. Thus the spectrum of the stationary source is

$$\bar{W}(\boldsymbol{\rho}_1, \boldsymbol{\rho}_2, \omega) = e^{-\frac{(\omega-\omega_c)^2}{2\sigma^2}}, \tag{4.1}$$

[1]This chapter is based on R.W. Schoonover, B.J. Davis, R.A. Bartels, P.S. Carney, "Optical interferometry with pulsed fields," *Journ. Mod. Opt.* **55**, 1541–1556 (2008).

where σ defines the effective bandwidth of the source and ω_c is the center frequency of the light. The shutter function (modulation) is likewise taken to be a Gaussian with effective pulse time T, *viz.*,

$$h_p(t) = e^{-\frac{t^2}{2T^2}}. \tag{4.2}$$

These pulses are the so-called Gaussian-Schell model pulses [31].

When T_0 is much larger than $\tau_c \approx 1/\sigma$ and T (*i.e.*, Regimes II & III), only fields within individual pulses exhibit a non-zero correlation. Thus, the overlap at the screen between pulses can be ignored and $h_p(t)$ can replace $h(t)$ in the calculation. An additional simplification, that the fractional bandwidth σ/ω_c is sufficiently small, and some calculation yield the normalized mutual coherence function at the screen $\mathcal{A}$,

$$\Gamma_{\mathcal{A}}(z, z, t, t + t_d) = \exp\left[-\frac{(2t + t_d - 2z/c)^2}{4T^2}\right] \exp\left[-\frac{t_d^2}{2\Delta^2}\right] \exp(-i\omega_c t_d), \tag{4.3}$$

where

$$\begin{aligned} \Delta^2 &= \frac{2T^2}{1 + 2\sigma^2 T^2}, \\ &= \frac{2T^2\tau_c^2}{\tau_c^2 + 2T^2}. \end{aligned} \tag{4.4}$$

Note that in Regime III, Eq. (4.4) is approximated by taking $\Delta^2 \approx \tau_c^2$, *i.e.*, the autocorrelation is dominated by the properties of the underlying stationary stochastic field. In Regime I, $\Delta^2 \approx 2T^2$ and the autocorrelation is then dominated by the effect of the pulsed modulation.

Any real measurement of the intensity at the detector involves an integration over the time, t. By assuming that the order of the temporal integration and the expectation operator can be interchanged, the expected measurement can be found by integrating Eq. (3.1) over all time. The expected normalized detector-integrated intensity pattern on

the screen is shown to be

$$\begin{aligned} I(P) &= \int_{-\infty}^{\infty} \mathrm{d}t\, \Gamma_{\mathcal{D}}(P,P,t,t) \\ &= 1+\exp(-t_d^2/2\Delta^2)\cos(\omega_c t_d), \end{aligned} \tag{4.5}$$

where t_d is the difference in propagation times from the two pinholes, *i.e.* $t_d = (R_2 - R_1)/c$. In order to achieve a stable, meaningful measurement, the variance of $I(P)$ about its mean must go to zero, *i.e.* cycloergodicity is assumed [40]. In deriving Eq. (4.5), slow detection was assumed, *i.e.*, the detector integration time is much larger than any other time scale in the system.

Plots of the detector-integrated intensity are shown in Figs. 4.1 and 4.2. In Fig. 4.1, the shape of the interferogram is mainly determined by the coherence time ($\tau_c \approx 1/\sigma$). The pulse time, T, is not a factor in the interference pattern (although it affects the total recorded intensity). In Fig. 4.2, the shape of the interferogram is mainly determined by the pulse time, T. Despite the fact that the two figures represent fields in two separate regions of the parameter space, the resultant integrated intensity patterns are nearly indistinguishable at the detector. This result implies that an interferometric measurement cannot distinguish between coherence time of the original pulse and the shaping of that pulse through $h(t)$. Such an ambiguity mirrors one shown in the spectral domain in which fields that lie in different regimes of parameter space can have identical spectra [31].

Now consider the interference pattern produced when interference between multiple pulses may be recorded, *i.e.* Regime I. Similar calculations yield the intensity on the screen after many pulses,

$$\begin{aligned} I(P) &= 1+\sum_n \sum_m \exp\left(-\frac{(m-n)^2 T_0^2 \sigma^2}{2+4\sigma^2 T^2}\right) \\ &\times \exp\left[-\frac{\Delta^2}{2}\left(\frac{t_d}{\Delta^2}+\frac{(m-n)T_0}{2T^2}\right)^2\right]\cos(\omega_c t_d). \end{aligned} \tag{4.6}$$

This equation is valid as long as consecutive pulses do not overlap, *i.e.* when $T_0 > T$. It is noteworthy that consecutive pulses may create secondary interference patterns on the

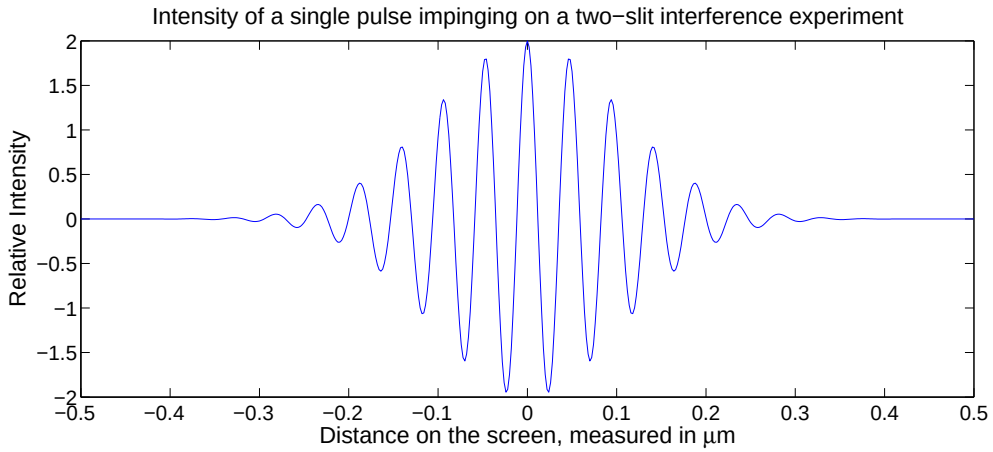

Figure 4.1: The interference pattern for a field with $\omega_c = 10^{15}$ rad/s, $T = 10$ fs, $\tau_c = 1/\sigma = 100$ fs, and $T_0 \gg \tau_c, T$, *i.e.*, Regime II. In this example, the pulse time is the dominant feature, as the coherence time is 10 times greater. Here, and in all other simulations, the distance between planes $\mathcal{A}$ and $\mathcal{D}$ is $d = 50$ mm.

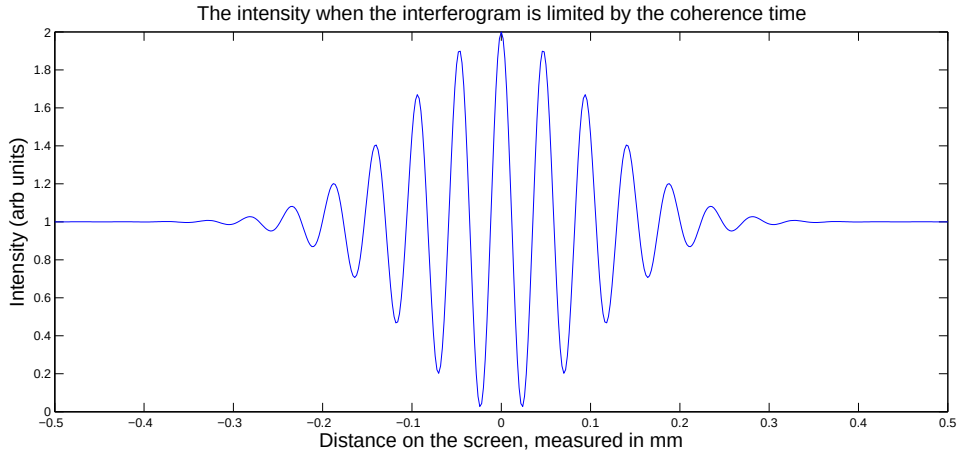

Figure 4.2: The interference pattern for a field with $\omega_c = 10^{15}$ rad/s, $T = 50\sqrt{2}$ fs, $\tau_c = 1/\sigma = 10\sqrt{2}$ fs and $T_0 \gg \tau_c, T$, *i.e.*, Regime III. In this example, the coherence time is the dominant feature, as the pulse time is 5 times greater.

screen spaced, in delay time, by multiples of the pulse period T_0. The primary interference pattern, occurring when $n = m$, represents the superposition of correlated fields within individual pulses. The secondary interference structures are due to the cross-correlation between the fields in pulses $m \neq n$, where $T_0|m - n|$ is the time delay between the two pulses. The number of the secondary interference patterns is dictated by the relevant regime. In Regime I, since the coherence time extends across multiple pulses, approximately τ_c/T_0 secondary interference structures will be present in the interference pattern. In Regimes II and III, only the primary interference structure will be present. The secondary interference patterns wash out with time-averaging because the fields in consecutive pulses are incoherent. In Fig. 4.3, an interferogram is shown with the same properties as Fig. 4.1, only with T_0 now small enough that consecutive pulses are within the coherence time of each other. One can see that smaller interference patterns show up next to the standard interference pattern in the center. The case where $\tau_c > T_0$ shows that consecutive pulses can have phase stability and hence produce predictable interference fringes. The repetition rate ($1/T_0$) is beyond what is currently realizable, but was chosen to show interpulse interference effects. Typical ultrafast pulsed lasers operate with repetition rate frequencies from tens of MHz to tens of GHz. However, a harmonically mode-locked diode laser has been demonstrated to operate at 500 GHz [47] ($T_0 = 2$ ps), which is similar to the values used in these simulations and is likely sufficient to observe interpulse effects.

The utility of a two-pinhole interferometer lies in the fact that the position on the screen maps directly to the time-difference coordinate. However, in the nonstationary case, the mutual correlation function depends also on an absolute time coordinate. The dependence on the absolute time coordinate reflects the fact that the deterministic shutter (modulation) samples the stationary stochastic field. Each pulse in the pulse train generates a distinct diffraction pattern, and the correlation that one might naively deduce from individual diffraction patterns (*i.e.*, modulus squared of the diffracted field) is not equivalent to the statistical correlation that one recovers with sufficient averaging. Time averaging by slow detectors effectively projects the mutual coherence onto the screen without any resolution of the absolute time coordinate. Even fast detectors can only approximately resolve the dependence on the absolute time coordinate, with a resolution

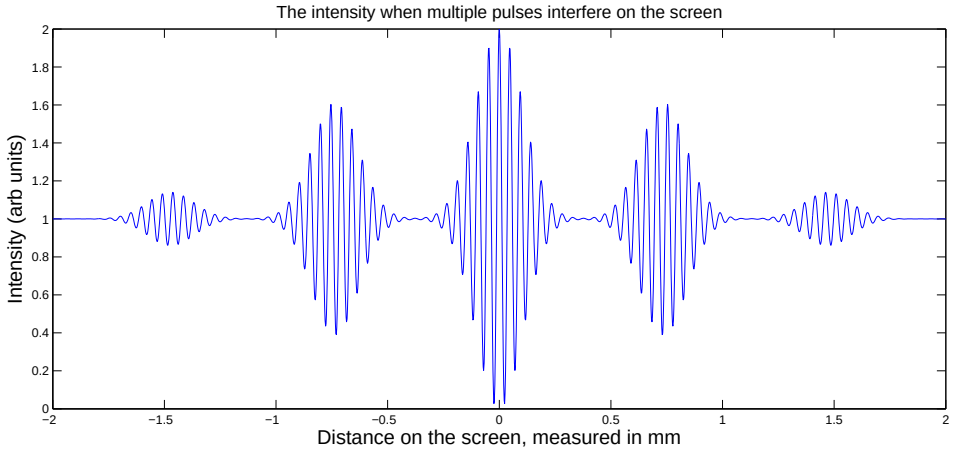

Figure 4.3: The interference pattern for a field with $\omega_c = 10^{15}$ rad/s, $T = 10$ fs, $\tau_c = 1/\sigma = 100$ fs, and $T_0 = 100$ fs, *i.e.* Regime I. In this example, the coherence length is the dominant feature, as the pulse length is 10 times greater. Multiple pulses can be seen to interfere on the screen.

determined by the integration time of the detector. Thus, the absolute time-dependence in Γ is often lost when performing an interference experiment. Without knowledge of the dependence on both time variables, one can no longer use Fourier transform relations to unambiguously map the spectrum [see Eq. (4.1)] to the detected intensity [see Eq. (4.6)]. Information regarding pulse duration, stability and repetition rate is now mixed in an underdetermined fashion and thus T, T_0, and τ_c cannot be resolved uniquely.

4.2 Simulations and Discussion

Results from the previous section for average quantities can be verified through numerical simulations of realizations of the ensemble of the random field. In particular, simulations show that time-averaged measurements coincide with the predicted measurements, validating the assumption of cycloergodicty used in Eq. (4.5). Following the strategy presented in [48], realizations of a discrete random process are used to simulate the source. A complex, white, Gaussian random process is simulated using a random number generator and then fed into a linear shift-invariant filter so that the output random process has the spectrum given in Eq. (4.1). This process is then shuttered to produce a pulsed field. The

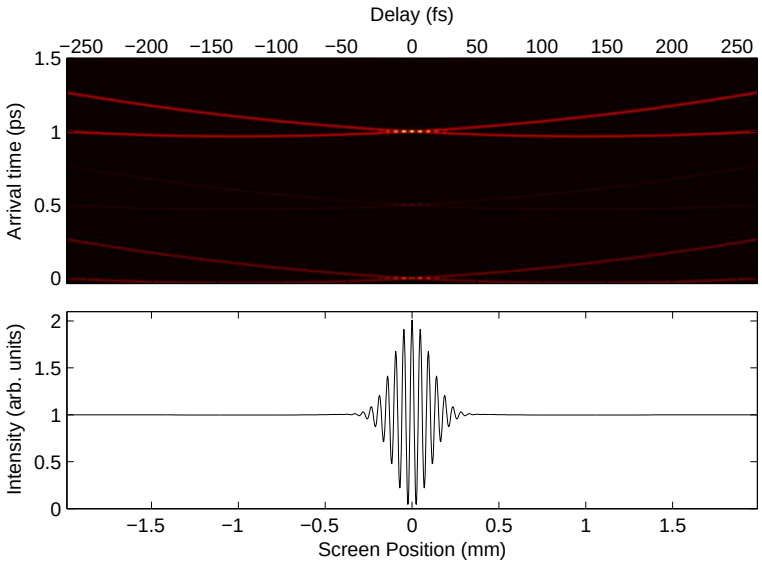

Figure 4.4: A simulation with T=10 fs, T_0=500 fs, τ_c=100 fs and $\omega_c = 10^{15}$ rad/s with 100 pulses measured. The top plot shows the instantaneous intensity as a function of screen position and time. The bottom plot is the average of the signal over the full 100 pulses. See Fig. 4.1 for analytic results.

signal at a given point on the screen, neglecting propagation factors, can then be found by taking two copies of the field, offsetting each in time by an amount corresponding to the pinhole-to-screen distance, and taking the square magnitude of their sum. The result gives the intensity on the screen as a function of time and with a temporal resolution higher than what is currently achievable experimentally. The appropriate time averages are then implemented to simulate measurable quantities.

In these simulations, pulses are created by realizing the underlying stationary process $\bar{U}(t)$. Simulations of the scenarios shown in Figs. 4.1, 4.2 and 4.3 are shown in Figs. 4.4, 4.5 and 4.6 respectively. There is good agreement between the simulations and the analytic results. The instantaneous intensity is shown as a function of screen position and time in the upper plot, and the time average as a function of position is shown in the lower plot. These simulations provide an alternative numerical means to calculate measurable quantities at the screen. One can also attain representative fields that are not accessible either via measurement or through analytic calculations based only on second-order statistics. The intensity of such a representative field is shown in the upper plots of Figs. 4.4, 4.5 and 4.6. One notices that each pair of overlapping pulses produces an

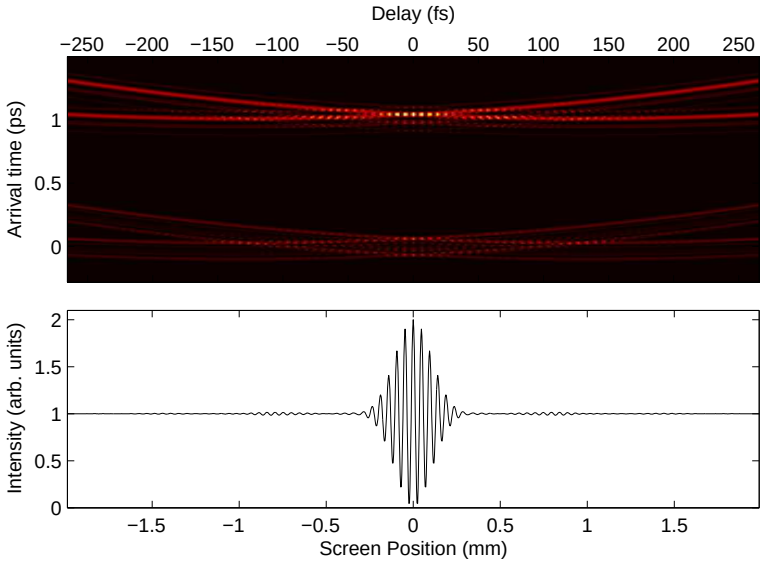

Figure 4.5: A simulation with $T = 50\sqrt{2}$ fs, T_0=500 fs, $\tau_c = 10\sqrt{2}$ fs and 100 pulses measured. Speckle-like effects, where different parts of the pulse interfere with each other, are visible in the upper plot. There is only phase-stability around the coherence length. This is the case where the pulsed nature is unimportant as $\tau_c < T$. See Fig. 4.2 for analytic results.

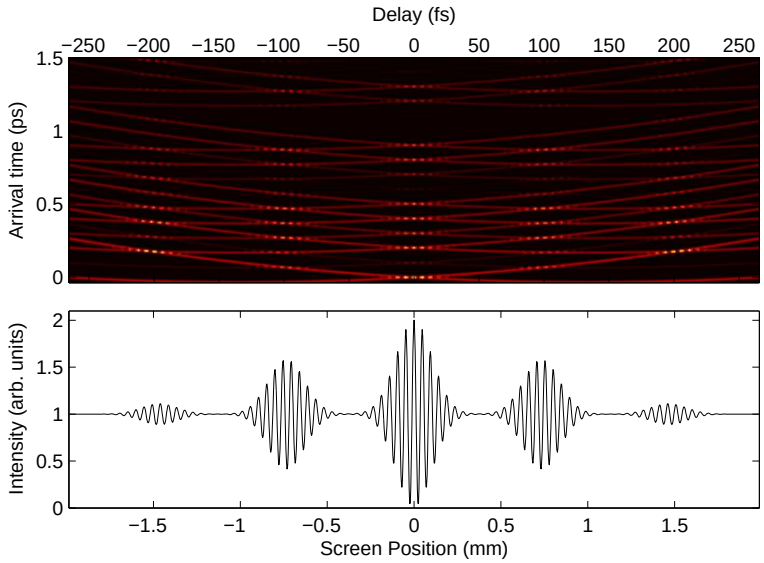

Figure 4.6: A simulation with the parameters T=10 fs, T_0=100 fs, τ_c=100 fs and 500 pulses. Interpulse interference is now stable. Secondary fringe structures are thus present. See Fig. 4.3 for analytic results.

oscillatory intensity pattern, but these should not be confused with interference patterns. Magyar and Mandel showed previously that uncorrelated light can create diffraction patterns that look like interference [7], but as they rightly concluded, this is not a statistical effect. As seen in the figures, many of these features wash out due to instability in the fringe position. Only the fields displaying coherence (or at least partial coherence) have the stable phase structure that allows the oscillations to survive the time averaging.

The interference pattern in a Young's two-pinhole experiment has been examined in the context of pulsed, stationary fields. Three time scales are important in such fields: the coherence time, the pulse time, and the interpulse time. Analytic results illustrate an equivalence between interferograms from different regimes and predict multipulse interference effects. Numerical simulations verify these results.

CHAPTER 5

THE GENERALIZED WOLF SHIFT

In which the Wolf shift is generalized,
and an experiment is performed

It has been shown that, for stationary optical sources, the power spectrum may undergo correlation-induced changes on propagation, the so-called Wolf shift [49, 50]. In this chapter, changes in the generalized power spectra and the two-frequency cross-spectral density are predicted for fields generated by cyclostationary sources. Examples illustrate these effects, and a novel detection scheme is proposed for detecting and determining individually the correlation-dependent changes in the generalized spectra upon propagation. An experiment using acoustic fields is used to verify the results.[1]

5.1 The Wolf Shift for Stationary Fields

It is well known that optical sources emit fields that, upon propagation, have a different spectrum than that of the original source. For statistically stationary optical sources, this propagation-induced effect has been shown to be a function of the coherence properties of the source [49]. Consider a stationary source that has a well-defined spectrum, $S(\omega)$, but has non-trivial correlations throughout the source. Thus, the cross-spectral density has the form

$$\bar{W}(\mathbf{r}_1, \mathbf{r}_2, \omega) = B(\mathbf{r}_1, \mathbf{r}_2) S(\omega). \tag{5.1}$$

[1]This chapter is based on R.W. Schoonover, B.J. Davis, P.S. Carney, "The generalized Wolf shift for cyclostationary fields," *Opt. Express* **17**, 4705–4711 (2009).

Using the far-field approximation to the propagator, K, in Eq. (A.17), one sees that the measured spectrum in the far zone of the source is

$$S^{(\infty)}(\mathbf{r},\omega) = \frac{\mathcal{W}(-k\hat{r}, k\hat{r}, \omega)}{r^2}, \tag{5.2}$$

where $\mathcal{W}$ is the six-dimensional Fourier transform of $\bar{W}$. Inserting Eq. (5.1) in to Eq. (5.2), the measured spectrum is found to be

$$S^{(\infty)}(\mathbf{r},\omega) = S(\omega)\frac{\mathcal{B}(-k\hat{r}, k\hat{r})}{r^2}. \tag{5.3}$$

The factor $\mathcal{B}$ is a function of the coherence properties of the source, and shifts the spectrum. This effect is known as the Wolf shift, and it has been experimentally verified in a number of experiments [51].

It has been shown that the Wolf shift is important in a number of applications. This propagation-induced, coherence-dependent shift can have the effect of red-shifting the spectrum of light from distant objects [52]. These results can come to bear on inferences on the rate of travel of distant galaxies and stars [53]. Certain types of scattering media can likewise create correlation-dependent shifts that resemble Doppler shifts [54]. The significance of the Wolf shift for radiometry measurements has been well studied, as well [55].

5.2 Propagation of the Generalized Spectra of Cyclostationary Fields

For a stochastic, cyclostationary source $Q(\mathbf{r},t)$, the mutual coherence function is

$$\begin{aligned} \Gamma_Q(\mathbf{r}_1,\mathbf{r}_2,t-\tau,t) &= \langle Q^*(\mathbf{r}_1,t-\tau)Q(\mathbf{r}_2,t)\rangle, \\ &= \sum_n Q_n(\mathbf{r}_1,\mathbf{r}_2,\tau)e^{-i\omega_0 nt}, \end{aligned} \tag{5.4}$$

where the brackets denote an ensemble average. Cycloergodicity is assumed, so the appropriate ensemble averages and long time averages are equivalent. The generalized cross-spectra are given by

$$W_Q(\mathbf{r}_1, \mathbf{r}_2, \omega, \omega + \omega) = \sum_n \tilde{Q}_n(\mathbf{r}_1, \mathbf{r}_2, \omega)\delta(\Omega - n\omega_0). \tag{5.5}$$

The measurement of the standard spectrum, where $\Omega = 0$, may be accomplished by means such as grating spectroscopy or Fourier transform spectroscopy. The spectral density of a cyclostationary source, secondary source, or field is given by the expression $S(\mathbf{r}, \omega) = W(\mathbf{r}, \mathbf{r}, \omega, \omega)$ [30], which implies that for cyclostationary fields the spectrum as would be measured in a standard spectrometer is given by the zeroth-order generalized spectra $S(\mathbf{r}, \omega) = \tilde{Q}_0(\mathbf{r}, \mathbf{r}, \omega)$ [36]. The generalized spectra and cross-spectra may be measured by heterodyne techniques, as is described near the end of this chapter.

In general, the spectrum, or for cyclostationary processes, the generalized spectra, cannot be determined at arbitrary points from the known spectra of the source or even the spectra on some plane. Instead, it is necessary to propagate the two-point, and for nonstationary processes, two-frequency, cross-spectral density. It has been shown that the two-point, two-frequency cross-spectral density satisfies the Wolf equation [2, 33],

$$(\nabla_1^2 + k_1^2)(\nabla_2^2 + k_2^2)W_R(\mathbf{r}_1, \mathbf{r}_2, \omega, \omega + \Omega) = (4\pi)^2 W_Q(\mathbf{r}_1, \mathbf{r}_2, \omega, \omega + \Omega), \tag{5.6}$$

where W_Q is the source cross-spectral density and W_R is the cross-spectral density for the radiated field, $k_1 = \omega/c$ and $k_2 = (\omega + \Omega)/c$. As shown in Appendix A, the radiated field can thus be found by the method of Green functions, and the cross-spectral density for the radiated field in the far zone takes the form

$$W^{(\infty)}(\mathbf{r}_1, \mathbf{r}_2, \omega, \omega + \Omega) = \frac{e^{i(k_2 r_2 - k_1 r_1)}}{r_1 r_2} \mathcal{W}_Q(-k_1 \hat{r}_1, k_2 \hat{r}_2, \omega, \omega + \Omega), \tag{5.7}$$

where $\mathbf{r}_i = r_i \hat{r}_i$ and $\mathcal{W}_Q$ is the six-dimensional spatial Fourier transform of W_Q. For stationary fields [49], the peak of the spectrum of the radiated field generally shifts

compared to the source spectrum as a direct consequence of the correlations in the source. From Eqs. (5.5) and (5.7) and using the sifting property of the δ-function, one obtains

$$\begin{aligned} W^{(\infty)}(\mathbf{r}_1, \mathbf{r}_2, \omega, \omega + \Omega) &= \sum_n \frac{e^{i(k_{2,n} r_2 - k_1 r_1)}}{r_1 r_2} \tilde{\mathcal{Q}}_n(-k_1 \hat{r}_1, k_{2,n} \hat{r}_2, \omega) \\ &\times \delta(\Omega - n\omega_0), \end{aligned} \tag{5.8}$$

where $k_{2,n} = (\omega + n\omega_0)/c$ and $\tilde{\mathcal{Q}}_n$ is the six-dimensional spatial Fourier transform of $\tilde{Q}_n$. Note that Eq. (5.8) is of the same form as Eq. (5.5), with generalized cross-spectra $\tilde{C}_n(\mathbf{r}_1, \mathbf{r}_2, \omega) = \exp(ik_{2,n} r_2 - ik_1 r_1)\tilde{\mathcal{Q}}_n(-k_1 \hat{r}_1, k_{2,n} \hat{r}_2, \omega)/r_1 r_2$. Because $\tilde{\mathcal{Q}}_n$ and $k_{2,n}$ differ for each n, each generalized spectrum may experience a different spectral shift. Thus the standard Wolf shift may be seen in the different forms of $\tilde{C}_0$ and $\tilde{Q}_0$, and a sequence of generalized Wolf shifts may be seen in each of these generalized spectra. This is the main result of this chapter, which will now be illustrated through example. The measured spectrum in the far zone is given by

$$S^{(\infty)}(\mathbf{r}, \omega) = \frac{\tilde{\mathcal{Q}}_0(-k\hat{r}, k\hat{r}, \omega)}{r^2}. \tag{5.9}$$

Equation (5.9) is of the same form as the propagation rule for the spectrum in the stationary case [2], where $\tilde{\mathcal{Q}}_0$ takes the place of the one-frequency cross-spectral density. There is no equivalent expression for the propagation rule for the generalized spectra in the theory of stationary fields. It is also important to note that all of the generalized spectra contribute to the optical intensity $I(\mathbf{r}, t) = \Gamma(\mathbf{r}, \mathbf{r}, t, t)$, and thus to the propagated pulse shape.

5.3 Intrinsically Stationary Model for Cyclostationary Fields

For an intrinsically stationary, cyclostationary optical field, the generalized Wolf shift takes a simplified form. Inserting Eq. (2.16) into Eq. (5.9), the measured spectrum in the far

zone is found to be

$$S^{(\infty)}(\mathbf{r},\omega) = \frac{1}{r^2}\sum_n |h_n|^2 \bar{\mathcal{W}}_Q(-k\hat{r}, k\hat{r}, \omega - n\omega_0), \tag{5.10}$$

where $\bar{\mathcal{W}}$ is the six-dimensional Fourier transform of the stationary cross-spectral density of the source $\bar{W}$ and $k = \omega/c$. The modulation and the propagation both affect the spectrum in the far zone in a complicated manner for a general source. When the source can be factorized $\bar{W}(\mathbf{r}_1, \mathbf{r}_2, \omega) = A(\omega)D(\mathbf{r}_1, \mathbf{r}_2)$, the effects of modulation and propagation can be separated:

$$S^{(\infty)}(\mathbf{r},\omega) = \frac{\mathcal{D}(-k\hat{r}, k\hat{r})}{r^2}\sum_n |h_n|^2 A(\omega - n\omega_0). \tag{5.11}$$

The original spectrum, A, is broadened by the modulation, and then shifted in the course of propagation as a result of the factor $\mathcal{D}$.

As an example, consider a collection of M point-sources that are identically modulated. The source density for this system is given by the expression

$$Q(\mathbf{r},t) = \sum_{n=-\infty}^{\infty}\sum_{p=1}^{M} Q_p(t) h_n \exp(-in\omega_0 t)\delta^{(3)}(\mathbf{r} - \mathbf{r}^{(p)}), \tag{5.12}$$

where $Q_p(t)$ is the source density at point $\mathbf{r}^{(p)}$. The underlying sources, Q_p, are assumed to be partially correlated, stationary, random processes. The frequency-domain correlation function for the $\{Q_p\}$ is written as

$$\langle \tilde{Q}_p^*(\omega)\tilde{Q}_q(\omega')\rangle = S(\omega)\mu_{pq}(\omega)\delta(\omega - \omega'), \tag{5.13}$$

where $\langle\cdot\rangle$ denotes an ensemble average and μ_{pq} is the spectral degree of coherence between the point sources at $\mathbf{r}^{(p)}$ and $\mathbf{r}^{(q)}$, respectively. Each point source is taken to have the same spectrum, $S(\omega)$. The field radiated from the collection of modulated sources has a

two-frequency cross-spectral density

$$W^{(\infty)}(\mathbf{r}_1,\mathbf{r}_2,\omega,\omega+\Omega) = \sum_{m,n}\sum_{p,q=1}^{M} h_n^* h_{m+n} \frac{e^{-ik_1|\mathbf{r}_1-\mathbf{r}^{(p)}|}}{|\mathbf{r}_1-\mathbf{r}^{(p)}|}\frac{e^{ik_{2,m}|\mathbf{r}_2-\mathbf{r}^{(q)}|}}{|\mathbf{r}_2-\mathbf{r}^{(q)}|} \times S(\omega-n\omega_0)\mu_{pq}(\omega-n\omega_0)\delta(\Omega-m\omega_0). \quad (5.14)$$

In Fig. 5.1 the normalized spectra, $\tilde{C_0}$ and $|\tilde{C_4}|$, are shown at both the sources and at a point far away for a collection of three sources, located along the x-axis at $x = 100$ mm, $x = 0$ mm, and $x = -100$ mm, respectively. The $\{h_n\}$ represent a square wave with a 10% duty cycle, $S(\omega)$ is taken to be a Gaussian function with 20% bandwidth and center frequency $\omega_c = 5 \times 10^{15}$ rad/s, and the spectral degree of coherence is taken to be

$$\mu_{ij}(\omega) = \begin{cases} 1 & i = j \\ \mu \exp\left(-\frac{(\omega-\omega_c)^2}{2\chi^2}\right) & i \neq j, \end{cases} \quad (5.15)$$

where χ is the bandwidth of the coherence function, assumed to be the bandwidth of the spectrum for this example. In the top two panels, the normalized generalized spectra for $\tilde{C_0}$ and $|C_4|$ are shown for sources that are highly correlated ($\mu = 0.8$). The middle two panels show simulations of the same system as in the top two panels, except that the sources are less correlated ($\mu = 0.1$). The peak frequencies for both $\tilde{C_0}(\omega)$ and $|\tilde{C_4}(\omega)|$ are each less red-shifted in the lower-coherence case. In the bottom panels of Fig. 5.1, $\tilde{C_0}$ and $|C_4|$ are shown for the same system as in the middle two panels, except that the repetition rate of the system has been changed from 1% of the center frequency to 5% of the center frequency. In this case, the length of the pulse is two optical cycles. Note that while the plot for $\tilde{C_0}$ is only slightly changed on propagation at the higher repetition rate, the plot for $\tilde{C_4}$ is much changed, with the secondary peak red-shifted instead of blue-shifted from the primary peak.

The example above may be realized in experiments in which a partially spatially coherent, cyclostationary, optical field illuminates small, point-like objects, for example in imaging of nanoparticles and quantum dots [56, 57, 58]. The objects are then secondary sources, and the field scattered from those objects can exhibit shifts in the generalized

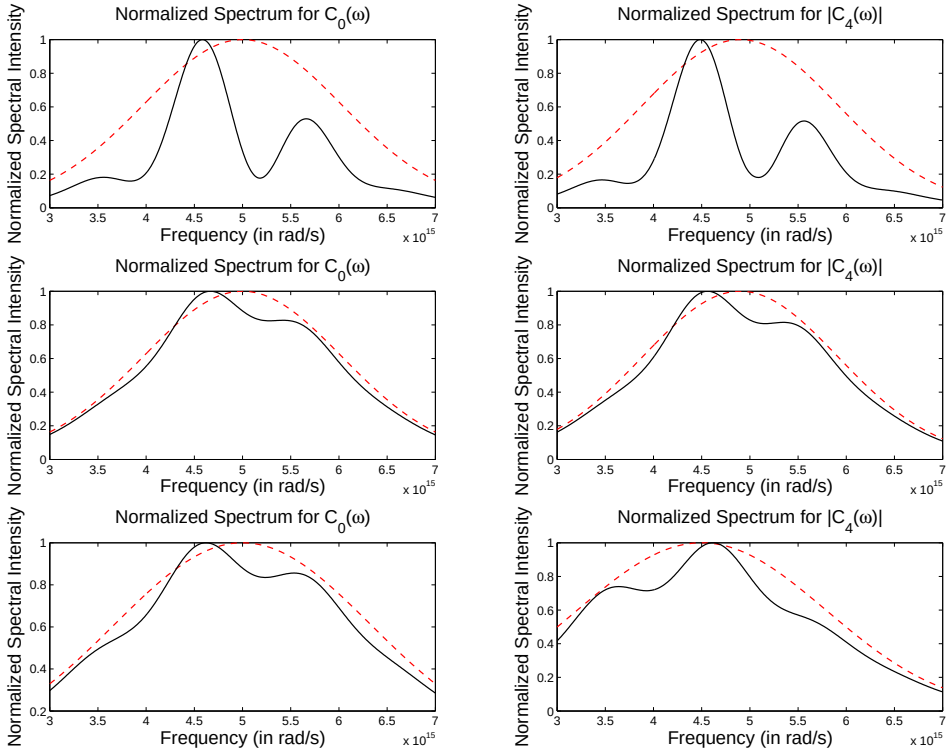

Figure 5.1: The normalized spectral density, $\tilde{C}_0(\omega)$, is shown on the left and the spectral correlation function $|\tilde{C}_4(\omega)|$ normalized by its peak on the right, at the source (dashed lines in red) and at a point in the far zone $P = (100, 0, 12000)$ mm (in black) for the case when there are three sources. In the top row, plots for a three-source system with $\mu = 0.8$, a repetition frequency of 5×10^{13} rad/s, and the bandwidth of the coherence and the bandwidth of the spectrum at 20% of the center frequency $\omega_c = 5 \times 10^{15}$ rad/s are shown. The middle row contains plots for the same three-source system as above, only with $\mu = 0.1$. The bottom row contains plots for a three-source system that differs from that in the middle panels by changing the repetition frequency from 5×10^{13} rad/s to 2.5×10^{14} rad/s.

spectra.

As another model for the generation of cyclostationary light, consider a mode-locked laser in which the carrier envelope has phase fluctuations. The electric field at the output of a mode-locked laser can be modeled by $U(\mathbf{r},t) = f(\mathbf{r})\sum_n A_n \exp[i(\omega_c + n\omega_0)t]$ [59], where $\{A_n\}$ describe the periodic envelope around the carrier wave centered at ω_c. While in the idealized case the phase between the carrier wave and the envelope can be perfectly matched [60], in reality, there is some random phase between the output comb lines. The $\{A_n\}$ are random coefficients with correlation matrix $\alpha_{nm} = \langle A_n^* A_m \rangle$. The two-frequency cross-spectral density at the output plane can be put in the form of Eq. (5.5) with

$$\tilde{C}_m(\mathbf{r}_1, \mathbf{r}_2, \omega) = F(\mathbf{r}_1, \mathbf{r}_2) \sum_n \alpha_{n\,n+m} \delta(\omega - \omega_c + n\omega_0) \tag{5.16}$$

and $F(\mathbf{r}_1, \mathbf{r}_2) = f^*(\mathbf{r}_1) f(\mathbf{r}_2)$. If the phase fluctuations at the output plane depend on position, the function $F(\mathbf{r}_1, \mathbf{r}_2)$ will not be separable and the source will be spatially partially coherent. The field that propagates away from the output plane will then exhibit the correlation-induced shifts presented in this chapter.

5.4 Experimental Evidence of Generalized Wolf Shifts

An acoustic experiment was performed to verify the correlation-dependence of propagation-induced changes in the spectra and cross-spectra for cyclostationary fields. Two unfocused circular pistons with nominal center frequency of 1 MHz and reported diameter of 0.125 inches, spaced apart by approximately 2 cm, were used as sources for a cyclostationary acoustic field. The acoustic field was measured on a third transducer: a 1 mm wide by 1 cm high rectangular transducer focused on elevation (focal number $f\#$ of 8) with nominal center frequency of 5 MHz (Valpey Fisher Corporation, Hopkinton, MA) approximately 20 cm away from the sources.

Two function generators were programmed according to Eq. (5.12), but with the limitation that there were 100 pulses (instead of an infinite number). The coefficients h_n were chosen to replicate a square wave with 10% duty cycle, the cyclostationary period was

chosen to be 100 μs, and the function $Q_p(t)$ was modeled as a Gaussian spectrum centered at 1 MHz with a coherence time of 120 μs in the manner of Section 4.2. The signals were generated in MATLAB and downloaded to two arbitrary waveform generators (Tabor Electronics models WW1281A and WW1281), one per transmitter transducer. Each signal generator was connected to a dedicated RF power amplifier (Model A150, 55 dB, 0.3-35 MHz and Model 2100L, 50 dB, 10 KHz - 12 MHz, ENI, Rochester, NY) in order to supply enough power to the transmitters. The echo signal from the rectangular transducer was received by a pulser-receiver (5800, Panametrics, Waltham, MA) and digitized by a 14-bit A/D card (UF3-4121, Strategic Test Corp., Woburn, MA) at 50 MHz. This field is consistent with being in Regime I. In the first experiment, μ_{12} was chosen to be 0.8; in the second experiment, μ_{12} was chosen to be 0.2, with μ_{12} defined by Eq. (5.13).

In Fig. 5.2, the correlation function $|C_0(\tau)|$ is plotted as a function of delay for the two experiments. Both plots show peaks in the correlation function every 100 μs, although of differing strengths. The 100 μs delay time between peaks matches the given cyclostationary period (repetition time) and the width of each correlation peak is 20 μs (or twice the pulse time). One sees that correlations exist between pulses separated by up to four temporal periods, and that individual pulses are strongly correlated with the pulses immediately behind and in front of them. The falloff in the strength of the correlations is consistent with the prescribed correlation properties.

In Fig. 5.3, the spectral density and the envelope of the spectral density are plotted for $\mu_{12} = 0.8$ (on the left) and $\mu_{12} = 0.2$ (on the right). All other properties of the field are held fixed. One sees immediately that the two spectral densities differ in both scaling and shape as a function of the spatial coherence properties. The envelopes are the same, as predicted by Eq. (5.11) . The displayed spectrum is consistent with Eq. (4.2): each spectral line is separated by 10 kHz (the repetition rate) and with varying peaks heights.

In Fig. 5.4, the magnitude of the cross-spectrum, $|\tilde{C}_4(\omega)|$, and the envelope of the cross-spectrum are plotted for $\mu_{12} = 0.8$ (on the left) and $\mu_{12} = 0.2$ (on the right). Again, the two plots differ both in terms of the underlying spectrum and the envelopes. In the case of the generalized spectrum, the envelope shape is dependent on the spectral degree of coherence of the collection of sources. Both correlations peak at 1.01 Mhz as opposed to

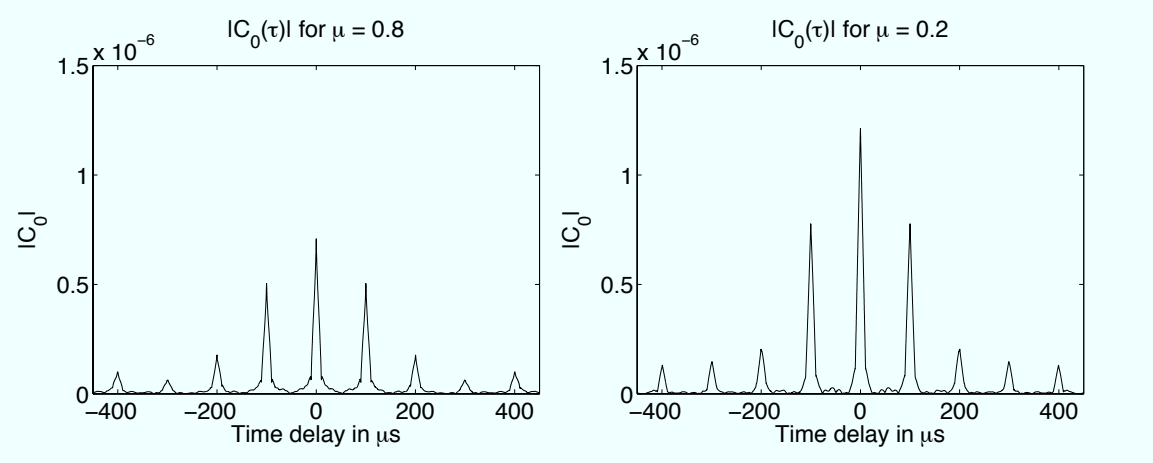

Figure 5.2: Plots of the correlation function, $|C_0(\tau)|$, for the experiment where the degrees of coherence between the fields emitted by the two transducers are 0.8 (left figure) and 0.2 (right figure). All other field parameters are the same for the fields associated with the two plots.

the peak of the spectrum at 1.00 MHz.

5.5 Interferometric Measurements of the Generalized Spectral Shifts for Optical Fields

Interferometric measurements are often made to determine the statistical properties of stationary fields. Because of the increase in the dimensionality in the case of cyclostationary fields (two time variables instead of one), conventional interferometric measurements must be augmented in some manner to make possible the inference of the statistical properties of the field [36]. For a cyclostationary field with correlation function $\Gamma(\boldsymbol{\rho}_1, \boldsymbol{\rho}_2, t-\tau, t) = \sum_m C_m(\boldsymbol{\rho}_1, \boldsymbol{\rho}_2, \tau) \exp(-im\omega_0 t)$ at the plane $z = 0$ of a Sagnac or Mach-Zehnder interferometer [61, see Ch. 2], the intensity at the output of the

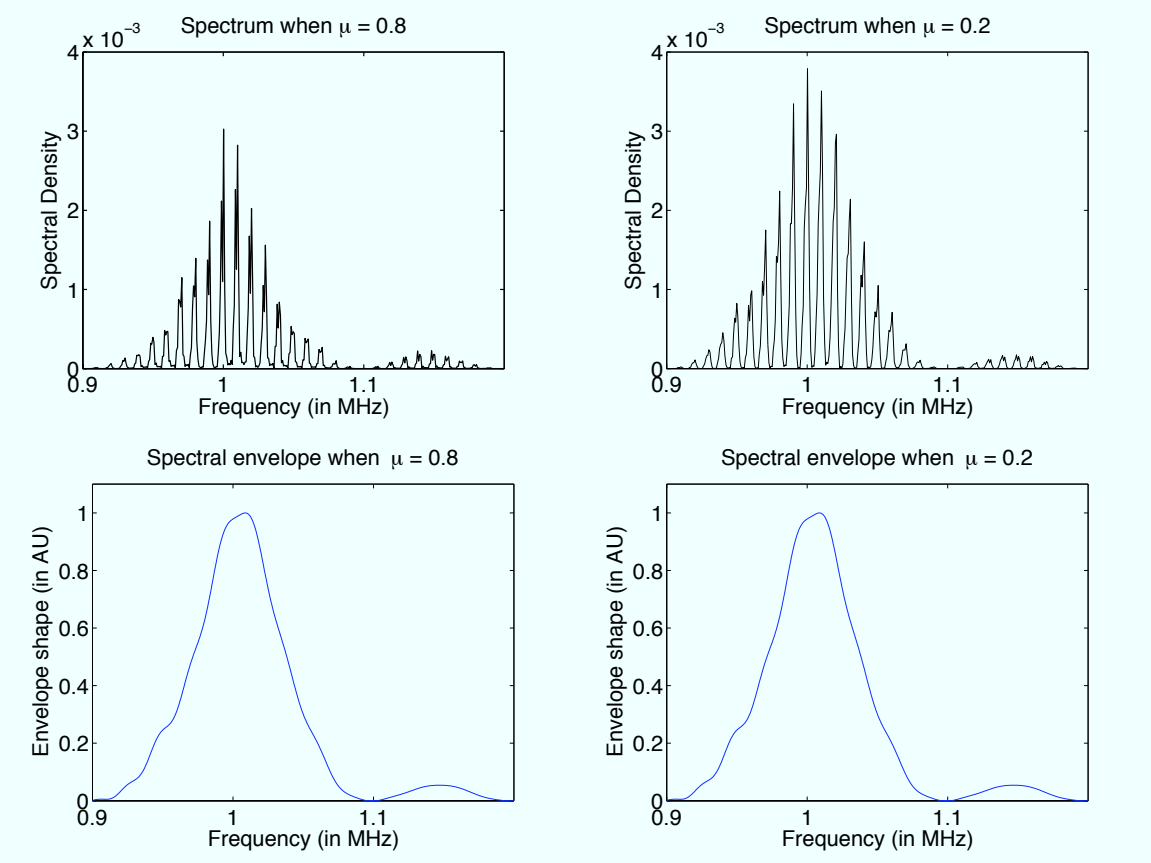

Figure 5.3: Plots of the spectral density, $\tilde{C}_0(\omega)$ (upper panels), and the envelope of the spectral density (lower panels) for the experiment where the degrees of coherence between the fields emitted by the two transducers are 0.8 (left panels) and 0.2 (right panels). All other field parameters are the same for the fields associated with the two plots.

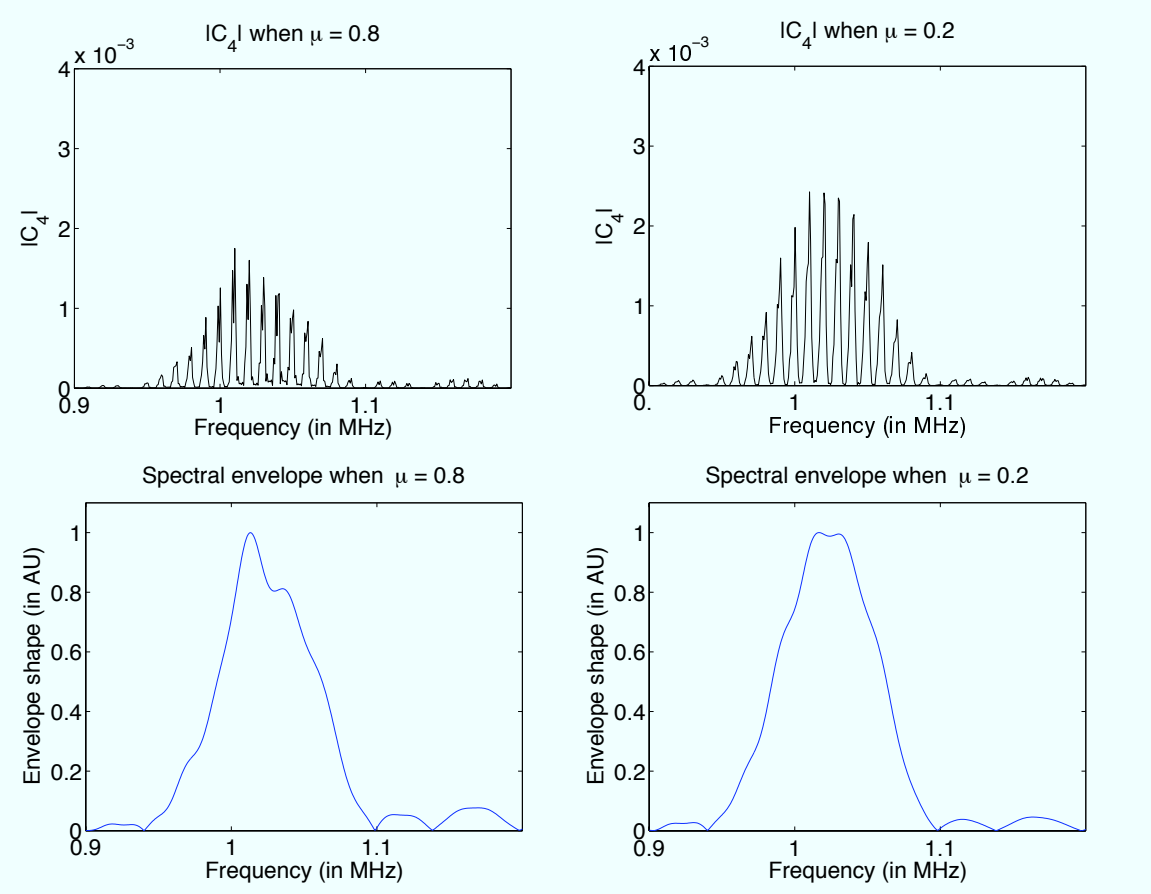

Figure 5.4: Plots of the cross-spectrum, $|\tilde{C}_4(\omega)|$ (upper panels), and the envelope of the cross-spectrum (lower panels) for the experiment where the degrees of coherence between the fields emitted by the two transducers are 0.8 (left panels) and 0.2 (right panels). All other field parameters are the same for the fields associated with the two plots.

interferometer is given by the expression

$$\begin{aligned} I(\boldsymbol{\rho},t;\tau) &\propto C_0(\boldsymbol{\rho},\boldsymbol{\rho},0)+|C_0(\boldsymbol{\rho},\boldsymbol{\rho},\tau)|\cos\alpha_0(\boldsymbol{\rho},\tau) \\ &+ 2\sum_{m=1}^{\infty}\{|C_m(\boldsymbol{\rho},\boldsymbol{\rho},0)|\cos\left(\frac{m\omega_0\tau}{2}\right)\cos[m\omega_0(t-\tau/2)-\alpha_m(\boldsymbol{\rho},0)] \\ &+ |C_m(\boldsymbol{\rho},\boldsymbol{\rho},\tau)|\cos[m\omega_0 t-\alpha_m(\boldsymbol{\rho},\tau)]+|C_{-m}(\boldsymbol{\rho},\boldsymbol{\rho},\tau)|\cos[m\omega_0 t+\alpha_{-m}(\boldsymbol{\rho},\tau)]\}, \end{aligned} \tag{5.17}$$

where $\boldsymbol{\rho}$ is the planar coordinate on the detector, $\alpha_m(\boldsymbol{\rho},\tau)=\arg[C_m(\boldsymbol{\rho},\boldsymbol{\rho},\tau)]$ and τ is the delay in one of the interferometer arms. Since the time dependence is purely sinusoidal, a heterodyne detection scheme [62, 63] at the output of the interferometer allows each term in the sum in Eq. (5.17) to be determined individually. In heterodyne detection, the electrical signal from a detector is mixed with a sinusoidal electrical signal (the local oscillator). The output of a heterodyne detector is the amplitude of the original signal at the frequency of the local oscillator. The local oscillator frequency may be tuned to values $m\omega_0 = 2\pi m/T_0$ to attain each term in Eq. (5.17).

At the observation plane of a Young's two-pinhole interferometer [43], the measured intensity of an incident cyclostationary field is given by the expression

$$\begin{aligned} I_{12}(t;\tau) &\propto C_0^{(11)}(0)+C_0^{(22)}(0)+2\left|C_0^{(12)}(\tau)\right|\cos\left[\alpha_0^{(12)}(\tau)\right] \\ &+ 2\sum_{m=1}^{\infty}\left\{|C_m^{(11)}(0)|\cos[m\omega_0(t-R_1/c)+\alpha_m^{(11)}(0)]\right. \\ &+ |C_m^{(22)}(0)|\cos[m\omega_0(t-R_2/c)+\alpha_m^{(22)}(0)] \\ &+ |C_m^{(12)}(\tau)|\cos[m\omega_0(t-R_2/c)+\alpha_m^{(12)}(\tau)] \\ &+ \left.|C_m^{(21)}(-\tau)|\cos[m\omega_0(t-R_1/c)+\alpha_m^{(21)}(-\tau)]\right\} \end{aligned} \tag{5.18}$$

where $C_m^{(ij)}(\tau)=C_m(P_i,P_j,\tau)$, P_i is the location of the pinhole i, $\alpha_m^{(ij)}(\tau)=\arg[C_m^{(ij)}(\tau)]$ and $\tau=(R_1-R_2)/c$, with R_i being the distance between the pinhole located at P_i. Again, a heterodyne detection scheme will yield each term in the sum in Eq. (5.18) individually. By varying the locations of the pinholes, the generalized correlation functions C_m may be recovered.

The correlation-induced changes in the field upon propagation are observable in the

detection scheme described above. Suppose the field with correlation function $\Gamma(\boldsymbol{\rho}, \boldsymbol{\rho}, t-\tau, t) = \sum_m C_m(\boldsymbol{\rho}, \boldsymbol{\rho}, \tau) \exp(-im\omega_0 t)$ on a plane $z = 0$ is allowed to propagate to a plane $z = z', z' \gg 0$ where another Mach-Zahnder interferometer is present. The intensity at the output of the interferometer is given by

$$\begin{aligned} r^2 I(\boldsymbol{\rho}, t; \tau) \;&\propto\; F_0(\hat{r}, 0) + |F_0(\hat{r}, \tau)| \cos\phi_0(\hat{r}, \tau) \\ &+\; 2\sum_{m=1}^{\infty} \left\{ |F_m(\hat{r}, 0)| \cos\left(\frac{m\omega_0\tau}{2}\right) \cos[m\omega_0(t - \tau/2 - r/c) - \phi_m(\hat{r}, 0)] \right. \\ &+\; |F_m(\hat{r}, \tau)| \cos[m\omega_0(t - r/c) - \phi_m(\hat{r}, \tau)] \\ &+\; \left. |F_{-m}(\hat{r}, \tau) \cos[m\omega_0(t - r/c) + \phi_{-m}(\hat{r}, \tau)] \right\} \end{aligned} \tag{5.19}$$

where $F_m(\hat{r}, \tau) = \frac{1}{2\pi} \int \tilde{\mathcal{C}}_m(-k_1\hat{r}, k_{2,m}\hat{r}, \omega) \exp(-i\omega\tau) \mathrm{d}\omega$, $\phi_m(\hat{r}, \tau) = \arg[F_m(\hat{r}, \tau)]$, r is the distance between the detector and the source, and the mapping between $\hat{r}$ and $\boldsymbol{\rho}$ is $\boldsymbol{\rho}/r = \hat{r}_\perp$. Heterodyne detection can then be used to find each term in the sum. The coherence-induced changes in the field can then be determined by comparison of the terms at frequency $m\omega_0$ at the planes $z = 0$ and $z = z'$.

In this chapter, it has been shown that the Wolf shift from the theory of stationary, partially coherent fields, can be seen as well in fields governed by the theory of cyclostationary, partially coherent random processes. In this more general setting, a new set of phenomena are predicted: distinct generalized Wolf shifts for each of the generalized spectra. The spectral correlation functions for cyclostationary fields, each representing a correlation between distinct frequencies, undergo separate shifts based on the repetition frequency of the system and the spatial properties of the source. These correlation-dependent, propagation-induced shifts will each contribute individually to changes in the measured intensity of the field far from the source, and may be seen individually in a combined interferometric-heterodyne detection scheme.

CHAPTER 6

THE STATE OF POLARIZATION FOR CYCLOSTATIONARY FIELDS

In which the extension to electromagnetic fields is considered and the state of polarization becomes obscured

---

In this chapter, cyclostationary electromagnetic fields are considered. The mutual coherence tensor for cyclostationary fields is introduced, as are the cyclostationary analogs of the Stokes parameters [64]. It is shown that the state of polarization of the cyclostationary electromagnetic field exhibits correlation-dependent, propagation-induced changes upon propagation.

6.1 Electromagnetic Fields and the Stokes Parameters

Up to this point, this dissertation has been concerned with the scalar model for optical fields. However, this model is not always sufficient to describe and characterize observed phenomena. Optical fields obey Maxwell's equations [65]: Constitutive relations [66] relate the field vectors ($\mathbf{E}$, $\mathbf{H}$) to the flux density vectors ($\mathbf{D}$, $\mathbf{B}$). In the case of propagation through non-dispersive, linear, isotropic and local media, Maxwell's equations imply the wave equation for the electric field:

$$\nabla \times \nabla \times \mathbf{E}(\mathbf{r}, t) + \frac{1}{c^2} \frac{\partial^2}{\partial t^2} \mathbf{E}(\mathbf{r}, t) = \mu_0 \mathbf{J}(\mathbf{r}, t). \tag{6.1}$$

Dyadic Green functions [67] based on Eq. (6.1) can be used to calculate the electric field away from a source.

When the field consists of plane waves directed in a small cone of angles about the z-axis, the field is said to be paraxial. In such cases, the field vectors lie approximately in the x-y plane. The study of the behavior of the electric field vector for paraxial fields is often described by the Stokes parameters [64]. The Stokes parameters are four numbers which uniquely specify the state of polarization of the electric field at a single point in space.

For time-harmonic fields, $\mathbf{E}(\mathbf{r},t) = \tilde{\mathbf{E}}(\mathbf{r})\exp(-i\omega t)$, the Stokes parameters are given by the following expressions:

$$S_0(\mathbf{r}) = |\tilde{E}_x(\mathbf{r})|^2 + |\tilde{E}_y(\mathbf{r})|^2 \tag{6.2}$$

$$S_1(\mathbf{r}) = |\tilde{E}_x(\mathbf{r})|^2 - |\tilde{E}_y(\mathbf{r})|^2 \tag{6.3}$$

$$S_2(\mathbf{r}) = 2\Re\{\tilde{E}_x^*(\mathbf{r})\tilde{E}_y(\mathbf{r})\} \tag{6.4}$$

$$S_3(\mathbf{r}) = 2\Im\{\tilde{E}_x^*(\mathbf{r})\tilde{E}_y(\mathbf{r})\}. \tag{6.5}$$

The parameter S_0 is proportional to the intensity of the electric field; the parameter S_1 characterizes the asymmetry in intensity between the two field components; and the parameters S_2 and S_3 characterize the relative phase between the two field components. For points at which $S_3 = 0$, the field is linearly polarized. For points at which $S_3 = \pm S_0$, the field is circularly polarized. The handedness of the field at a point is determined by the sign of S_3, with right-handed polarization states corresponding to $S_3 > 0$ and left-handed polarization states corresponding to $S_3 < 0$.

The state of polarization for a stationary field can be defined analogously to Eqs. (6.2)-(6.5) [3]. This formalism is often set in the frequency domain. It has been shown that for a stationary electromagnetic field, the state of polarization changes upon propagation [68]. A correlation-induced change in the state of polarization requires an anisotropy in either the correlation function [69] or the medium through which the field is propagating.

6.2 Cyclostationary Electromagnetic Fields

Analogously to the mutual coherence function for scalar optical fields [see Eq. (2.10)], a random, paraxial electromagnetic field, $\mathbf{E}(\mathbf{r}, t)$, has a mutual coherence tensor that is given by

$$\bar{\Gamma}(\mathbf{r}_1, \mathbf{r}_2, t_1, t_2) = \langle \mathbf{E}(\mathbf{r}_2, t_2)\mathbf{E}^\dagger(\mathbf{r}_1, t_1)\rangle, \tag{6.6}$$

where the angle brackets denote an ensemble average and the overbar denotes a matrix. The diagonal elements of the mutual coherence tensor give the mutual coherence function for each of the two components. The off-diagonal elements describe the cross-correlations between the x- and y-components of the electric field.

In many experiments, measurable quantities are related to the mutual coherence function of the field evaluated at $\mathbf{r}_1 = \mathbf{r}_2 = \mathbf{r}$ and $t_1 = t_2$. Because of this, the coherency matrix $\bar{J}$ has been introduced as shorthand [2, Chapter 6]. The coherency matrix is defined as

$$\begin{aligned} \bar{J}(\mathbf{r}, t) &= \langle \mathbf{E}(\mathbf{r}, t)\mathbf{E}^\dagger(\mathbf{r}, t)\rangle & (6.7)\\ &= \bar{\Gamma}(\mathbf{r}, \mathbf{r}, t, t). & (6.8) \end{aligned}$$

The coherency matrix is independent of time for fields obeying stationary statistics. The Stokes parameters [64] for the random field can be derived from the coherency matrix via the relation

$$S_\alpha(\mathbf{r}, t) = \mathrm{Tr}\left[\bar{J}(\mathbf{r}, t)\bar{\sigma}_\alpha\right], \tag{6.9}$$

where $\bar{\sigma}_\alpha$ are the Pauli matrices:

$$\bar{\sigma}_0 = \begin{bmatrix} 1 & 0 \\ 0 & 1 \end{bmatrix}, \tag{6.10}$$

$$\bar{\sigma}_1 = \begin{bmatrix} 1 & 0 \\ 0 & -1 \end{bmatrix}, \tag{6.11}$$

$$\bar{\sigma}_2 = \begin{bmatrix} 0 & 1 \\ 1 & 0 \end{bmatrix}, \tag{6.12}$$

$$\bar{\sigma}_3 = \begin{bmatrix} 0 & -i \\ i & 0 \end{bmatrix}. \tag{6.13}$$

The state of polarization at any point, $\mathbf{r}$, for a stationary field, is independent of time.

When the electromagnetic field obeys cyclostationary statistics, $\bar{\Gamma}(\mathbf{r}_1, \mathbf{r}_2, t_1, t_2) = \bar{\Gamma}(\mathbf{r}_1, \mathbf{r}_2, t_1 + T_0, t_2 + T_0)$ for some T_0. This periodicity admits a Fourier representation for the mutual coherence tensor

$$\bar{\Gamma}(\mathbf{r}_1, \mathbf{r}_2, t - \tau, t) = \sum_n \bar{C}_n(\mathbf{r}_1, \mathbf{r}_2, \tau) e^{-in\omega_0 t}, \tag{6.14}$$

where $\omega_0 = 2\pi/T_0$. By inserting the expression in Eq. (6.14) into Eqs. (6.8) and (6.9), one finds that for cyclostationary fields, the Stokes parameters are also periodic functions of time. This is the main result of this chapter. A method for determining the cyclostationary Stokes parameters at a point in space would be similar to the method developed in Section 5.5.

6.3 Propagation through Anisotropic Media

As an example of the cyclostationary Stokes parameters, consider the case of a linearly polarized, cyclostationary field incident on a biaxial crystal:

$$\mathbf{E}(\mathbf{r}, t) = a(t)h(t)\frac{\hat{x} + \hat{y}}{\sqrt{2}}, \tag{6.15}$$

where $a(t)$ is a stationary field with autocorrelation $\langle a^*(t)a(t+\tau)\rangle = A'(\tau)$ and $h(t)$ is a deterministic, periodic function. The product of a stationary field and a periodic field is cyclostationary. The periodic function h generally has the form $h(t) = \sum_m h_p(t - mT_0)$, where h_p describes the field for a single period. In the case of a periodically pulsed field, h_p is the pulse shape. The biaxial crystal is assumed to have the fast axis along the x-axis with index of refraction n_f, the slow axis along the y-axis with index of refraction n_s and thickness d.

The Stokes parameters for the pulsed field before the biaxial medium are given by

$$S_0(t) = A'(0)|h(t)|^2 \tag{6.16}$$

$$S_1(t) = 0 \tag{6.17}$$

$$S_2(t) = A'(0)|h(t)|^2 \tag{6.18}$$

$$S_3(t) = 0. \tag{6.19}$$

After passing through the medium, the Stokes parameters for the field are given by

$$S_0(t) = \frac{1}{2}A'(0)\left[|h(t - dn_f/c)|^2 + |h(t - dn_s/c)|^2\right] \tag{6.20}$$

$$S_1(t) = \frac{1}{2}A'(0)\left[|h(t - dn_f/c)|^2 - |h(t - dn_s/c)|^2\right] \tag{6.21}$$

$$S_2(t) = \Re\{A'\left[\frac{(n_s - n_f)d}{c}\right] h(t - dn_f/c)h^*(t - dn_s/c)\} \tag{6.22}$$

$$S_3(t) = \Im\{A'\left[\frac{(n_s - n_f)d}{c}\right] h(t - dn_f/c)h^*(t - dn_s/c)\}. \tag{6.23}$$

In Fig. 6.1 the Stokes parameters are shown for the output of the biaxial crystal at two distances, d, of propagation through the medium. The medium is characterized by indices of refraction $n_s = 1.38$ and $n_f = 1.23$. The two distances of propagation are $d = 6\,\mu$m and $d = 18\,\mu$m, corresponding to delays within the field in the x- and y-directions of 2.95 fs and 8.95 fs, respectively. The modulation function, h, describes a Gaussian pulse with temporal width (variance) of 10 fs and cyclostationary period of 100 fs. The unmodulated stationary autocorrelation, A', is given by $A'(\tau) = \exp(-\tau^2/2\tau_c^2)\exp(-i\omega_c\tau)$ where $\tau_c = 80$ fs and $\frac{\omega_c}{2\pi} = 1.1$ PHz. This field is consistent with being in Regime II.

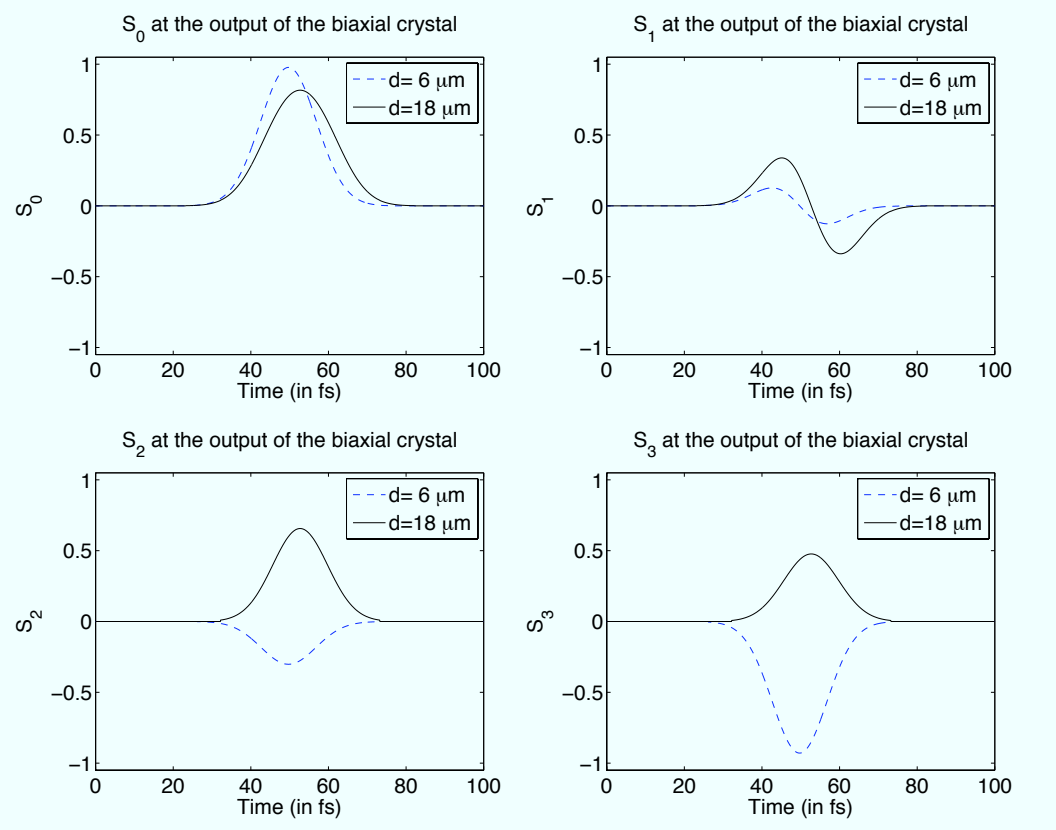

Figure 6.1: Plots of the cyclostationary Stokes parameters outputting from biaxial crystals of length $d = 6\,\mu$m (dashed blue lines) and $d = 18\,\mu$m (solid black lines). Both crystals have indices of refraction $n_s = 1.38$ and $n_f = 1.23$.

Although the pulsed fields in both cases contain the same amount of energy per pulse (the time integral of S_0 over the period), the distribution of that energy is a function of propagation distance. It is clear from the widths of S_0 in the upper left plot of Fig. 6.1 that the energy is spread out more after the longer propagation distance through the crystal. The upper right plot in Fig. 6.1 illustrates the fact that with the longer propagation distance through the crystal, the output field more closely resembles an x-polarized pulse followed closely by a y-polarized pulse. One sees that the handedness of the field (as determined by S_3) is different in the two cases. The incident field was linearly polarized, whereas the field exiting from the shorter crystal is left-handed and the field exiting from the longer crystal is right-handed. Likewise, the function S_2 changes sign for different propagation distances. By examining Eqs. (6.20)-(6.23), one notes that for

sufficiently large distances, d, the two components of the field will not overlap at all and $S_2(t)$ and $S_3(t)$ will be identically zero. In that case, $S_0(t)$ and $S_1(t)$ will possess two distinct regions in which the functions are non-zero: one associated with an x-polarized pulse and one associated with a y-polarized pulse.

In Table 6.1, the time-averaged values of the Stokes parameters are given for the two cases considered above. The time-averaged values of the Stokes parameters for cyclostationary fields correspond to what would be measured in any time-averaged detection system. The last row in Table 6.1 corresponds to the estimated difference in indices of refraction ($\delta n = n_s - n_f$) using the time-averaged Stokes parameters (for example, by inverting Eq. (31) in [70]). The real difference in indices of refraction is 0.15. Both estimates are off by a factor of five. Use of the cyclostationary Stokes parameters at any non-trivial time (whenever $S_0(t)$ is not zero) results in the correct estimation of δn.

Table 6.1: Time-averaged Stokes parameters for two propagation distances

	d_1	d_2
$\langle S_0 \rangle$	0.1771	0.1771
$\langle S_1 \rangle$	0	0
$\langle S_2 \rangle$	-0.0534	0.1159
$\langle S_3 \rangle$	-0.1645	0.0842
δn_{est}	0.8710	0.8684

In this chapter, the concept of the state of polarization is developed for cyclostationary fields. It is shown that the Stokes parameters are periodic functions of time. It is further shown that the propagation of a cyclostationary electromagnetic field can induce changes in the state of polarization of the field, and that this effect is correlation-dependent.

CHAPTER 7

CONCLUSIONS

In which the title says it all

In this dissertation, the theory of cyclostationary random processes is applied to the study of optical fields. While cyclostationary fields can describe a number of optical phenomena, the primary application is pulsed laser fields. A number of methods to generate pulse trains, including mode-locking, Q-switching, and high harmonic generation, may produce cyclostationary fields. The tools of cyclostationary analysis allow for the investigation of a number of coherence-dependent, propagation-induced effects. The effects that are investigated in this dissertation include interferometric, spectroscopic, and polarimetric measurements.

In Chapter 3, the interference patterns created by a spatially partially coherent cyclostationary field at various distances from the source are investigated. It is shown that standard interferometric techniques are not capable of fully recovering the correlation function of a cyclostationary field. It is shown that the spatial coherence properties of the primary source or secondary source can be determined only near that source.

The specific case of a spatially fully coherent, cyclostationary field illuminating an interferometer is investigated in Chapter 4. It is shown that by making measurements far from the source, where the field is spatially fully coherent, only the smaller of the coherence time and the pulse time may be inferred from the resulting interferograms.

In Chapter 5, spectroscopic measurements of cyclostationary fields are considred. It is shown that the spectrum and cross-spectra of a cyclostationary field exhibit correlation-dependent changes upon propagation. A proof-of-principle experiment was performed to verify the existence of correlation-dependent changes in the spectrum of

cyclostationary waves propagated from an acoustic source. A scheme for recovering the entire set of generalized correlation functions is proposed through the combination of heterodyne detection and interferometry.

Cyclostationary electromagnetic fields are shown to exhibit correlation-induced changes in their state of polarization upon propagation in Chapter 6. The state of polarization, as characterized by the Stokes parameters, is investigated. In the case of cyclostationary fields, the Stokes parameters are shown to be periodic functions of time. An example, based on wave propagation through a biaxial crystal, illustrates the changes in the Stokes parameters upon propagation.

Possible theoretical investigations of cyclostationary fields may include research on topics such as correlation-dependent changes in the field due to scattering; the manner in which the correlated spectra of cyclostationary fields affect the strength of nonlinear optical processes; and the extension of cyclostationarity to quantum optical processes. Combined work in theory and experiment might yield better models for cyclostationary fields beyond the intrinsically stationary model used in this dissertation.

APPENDIX A

PROPAGATION LAWS FOR TWO-POINT CORRELATION FUNCTIONS

In which second-order correlation functions are propagated for stationary and cyclostationary field models

---

In this appendix, the propagation law for nonstationary processes is derived. Certain restrictions apply to the form of the propagation laws when a specific type of statistic is specified. The well-known results for stationary fields, the Wolf equation and its spectral-domain analog, are derived. It is shown that in the case of cyclostationary fields, the double Helmholtz equation takes a restricted form.

In works on nonstationary fields [31, 32, 37], the emphasis has been on sources that are spatially fully coherent and of infinite extent. Such sources produce polychromatic plane waves. Real sources are of finite extent and can fluctuate independently at different points in space. An analysis of such partially spatially coherent sources and the fields they produce cannot be performed by analyzing polychromatic plane waves. Other works [32, 33] have dealt with spatial correlation functions of nonstationary fields within the context of coherent mode decompositions or the one-dimensional behavior of the two-frequency cross-spectral density function. Here, the propagation of partially spatially coherent cyclostationary statistical quantities is addressed.

For a general statistical field, any member of the ensemble that represents the random field obeys the wave equation

$$\left(\nabla^2 - \frac{1}{c^2}\frac{\partial^2}{\partial t^2}\right) V(\mathbf{r}, t) = -4\pi Q(\mathbf{r}, t), \tag{A.1}$$

where V is the field, c is the speed of light, and Q is the source of the optical field.

Re-writing the above equation with subscripts on the position and time coordinates, then taking the complex conjugate of the equation, yields

$$\left(\nabla_1^2 - \frac{1}{c^2}\frac{\partial^2}{\partial t_1^2}\right) V^*(\mathbf{r}_1, t_1) = -4\pi Q^*(\mathbf{r}_1, t). \tag{A.2}$$

Multiplying Eq. (A.2) by Eq. (A.1), with Eq. (A.1) now having the subscript "2" placed on all the independent variables, yields

$$\left(\nabla_1^2 - \frac{1}{c^2}\frac{\partial^2}{\partial t_1^2}\right)\left(\nabla_2^2 - \frac{1}{c^2}\frac{\partial^2}{\partial t_2^2}\right) V^*(\mathbf{r}_1, t_1)V(\mathbf{r}_2, t_2) = (4\pi)^2 Q^*(\mathbf{r}_1, t)Q(\mathbf{r}_2, t). \tag{A.3}$$

Averaging both sides over the ensemble, and interchanging the ordering of averaging and differentiation, results in

$$\left(\nabla_1^2 - \frac{1}{c^2}\frac{\partial^2}{\partial t_1^2}\right)\left(\nabla_2^2 - \frac{1}{c^2}\frac{\partial^2}{\partial t_2^2}\right) \Gamma_S(\mathbf{r}_1, \mathbf{r}_2, t_1, t_2) = (4\pi)^2 \Gamma_Q(\mathbf{r}_1, \mathbf{r}_2, t_1, t_2), \tag{A.4}$$

where Γ_S is the two-point, two-time mutual coherence function for the propagated field and Γ_Q is the two-point, two-time mutual coherence function for the optical source. In the case of stationary fields, only the time difference, $\tau = t_2 - t_1$, is relevant. When stationarity applies, Eq. (A.4) takes a slightly simplified form:

$$\left(\nabla_1^2 - \frac{1}{c^2}\frac{\partial^2}{\partial \tau}\right)\left(\nabla_2^2 - \frac{1}{c^2}\frac{\partial^2}{\partial \tau}\right) \Gamma'_S(\mathbf{r}_1, \mathbf{r}_2, \tau) = (4\pi)^2 \Gamma'_Q(\mathbf{r}_1, \mathbf{r}_2, \tau), \tag{A.5}$$

where the prime on Γ denotes a stationary random field as opposed to a general random field. Equation (A.5) is the so-called Wolf equation [71].

By understanding the differential equation that describes the spatio-temporal evolution of the quantity of interest—here, the mutual coherence function—one can construct a propagator, or Green function, that can be used to transform the differential equation into an integral equation [67]. The solution of the integral equation yields the mutual coherence function throughout a region of interest. In practice, it is often easier, both analytically and computationally, to propagate the members of the ensemble first, then perform the

average over the ensemble after propagation. In this case, one finds

$$V_S(\mathbf{r},t) = \int \mathrm{d}t'\,\mathrm{d}^3r'\,G(\mathbf{r},\mathbf{r}',t,t')V_P(\mathbf{r}',t') + \text{b.c.}, \tag{A.6}$$

where the causal Green function in free space is

$$G(\mathbf{r},\mathbf{r}',t,t') \;=\; \frac{\delta\left(t-t'-\frac{|\mathbf{r}-\mathbf{r}'|}{c}\right)}{|\mathbf{r}-\mathbf{r}'|}, \tag{A.7}$$

V_P is a member of the ensemble of the field at the source, V_S is the corresponding member of the ensemble propagated from the source, and b.c. stands for the terms resulting from satisfying boundary conditions. However, the averaging process may be carried out before propagation, in which case the Green function is given by

$$K(\mathbf{r}_1,\mathbf{r}_1',\mathbf{r}_2,\mathbf{r}_2',t_1,t_1',t_2,t_2') \;=\; G^*(\mathbf{r}_1,\mathbf{r}_1',t_1,t_1')G(\mathbf{r}_2,\mathbf{r}_2',t_2,t_2'). \tag{A.8}$$

The propagated second-order coherence function is then given by the integral equation

$$\begin{aligned}\Gamma_S(\mathbf{r}_1,\mathbf{r}_2,t_1,t_2) \;&=\; \int \mathrm{d}t_1'\,\mathrm{d}t_2'\,\mathrm{d}^3r_1'\,\mathrm{d}^3r_2'\,K(\mathbf{r}_1,\mathbf{r}_1',\mathbf{r}_2,\mathbf{r}_2',t_1,t_1',t_2,t_2') \\ &\times\; \Gamma_P(\mathbf{r}_1',\mathbf{r}_2',t_1',t_2'),\end{aligned} \tag{A.9}$$

where the terms related to boundary conditions have been omitted.

In many circumstances, even for deterministic fields, propagation of fields in the time domain is cumbersome. One technique for ameliorating this difficulty is to find the spectral representation of the field, propagate the field in the spectral domain, and then compute the propagated field or coherence function in the time domain. Using the generalization of the Wiener-Khintchine-Einstein theorem, and inserting the Fourier representations of Γ_S and Γ_Q into Eq. (A.4), one finds that the two-point, two-frequency cross-spectral density of an optical field obeys the differential equation

$$(\nabla_1^2 + k_1^2)(\nabla_2^2 + k_2^2)W_S(\mathbf{r}_1,\mathbf{r}_2,\omega_1,\omega_2) = (4\pi)^2 W_Q(\mathbf{r}_1,\mathbf{r}_2,\omega_1,\omega_2), \tag{A.10}$$

where $k_i = w_i/c$. Note that this result can also be found by constructing an ensemble of monochromatic fields that, when averaged, give W, and note that each member of the ensemble obeys the Helmholtz equation. One can construct a Green function for the differential equation that the cross-spectral density obeys, or one can construct the Green function for the Helmholtz equation that each member of the ensemble obeys. For the latter case, the propagated field is given by

$$\tilde{U}_S(\mathbf{r},\omega) = \int \mathrm{d}^3 r' \, \tilde{G}(\mathbf{r},\mathbf{r}';k)\tilde{U}_P(\mathbf{r}',\omega) + \text{b.c.}, \tag{A.11}$$

where the spectral Green function in free space is

$$\tilde{G}(\mathbf{r},\mathbf{r}';k) \;=\; \frac{e^{ik|\mathbf{r}-\mathbf{r}'|}}{|\mathbf{r}-\mathbf{r}'|}, \tag{A.12}$$

and $k = \omega/c$. If one chooses to carry out the operation of propagation after the averaging process, the appropriate integral equation is

$$\begin{aligned} W_S(\mathbf{r}_1,\mathbf{r}_2,\omega_1,\omega_2) \;&=\; \int \mathrm{d}^3 r_1' \, \mathrm{d}^3 r_2' \, \tilde{K}(\mathbf{r}_1,\mathbf{r}_1',\mathbf{r}_2,\mathbf{r}_2',\omega_1,\omega_2) \\ &\times\; W_P(\mathbf{r}_1',\mathbf{r}_2',\omega_1,\omega_2), \end{aligned} \tag{A.13}$$

where

$$\tilde{K}(\mathbf{r}_1,\mathbf{r}_1',\mathbf{r}_2,\mathbf{r}_2';k_1,k_2) \;=\; \tilde{G}^*(\mathbf{r}_1,\mathbf{r}_1';k_1)\tilde{G}(\mathbf{r}_2,\mathbf{r}_2';k_2). \tag{A.14}$$

In the case that the source is given on the plane $z = 0$ and there are no primary sources in the region $z \geq 0$, this reduces to

$$\begin{aligned} W_S(\mathbf{r}_1,\mathbf{r}_2,\omega_1,\omega_2) \;&=\; \frac{1}{(2\pi)^2} \iint_{z'=0} \mathrm{d}^2\rho_1' \mathrm{d}^2\rho_2' \, W_Q(\boldsymbol{\rho}_1',\boldsymbol{\rho}_2',\omega_1,\omega_2) \\ &\times\; \frac{\partial}{\partial z_1'} \frac{\partial}{\partial z_2'} K(\mathbf{r}_1,\mathbf{r}'_1,\mathbf{r}_2,\mathbf{r}'_2,k_1,k_2). \end{aligned} \tag{A.15}$$

Note that in the case of stationary fields, all frequencies are uncorrelated, and Eq. (A.10)

takes the form

$$(\nabla_1^2 + k^2)(\nabla_2^2 + k^2)W'_S(\mathbf{r}_1, \mathbf{r}_2, \omega)\delta(\omega - \omega') = (4\pi)^2 W'_Q(\mathbf{r}_1, \mathbf{r}_2, \omega)\delta(\omega - \omega'), \tag{A.16}$$

where the prime denotes that the functions W' are functions of one frequency. Equation (A.16) is the spectral domain analog of the Wolf equation. The resulting propagation law for the stationary fields is thus

$$\begin{aligned} W(\mathbf{r}_1, \mathbf{r}_2, \omega) &= \int \mathrm{d}^3 r'_1 \, \mathrm{d}^3 r'_2 \, \tilde{K}(\mathbf{r}_1, \mathbf{r}'_1, \mathbf{r}_2, \mathbf{r}'_2, \omega) \\ &\times \; W(\mathbf{r}'_1, \mathbf{r}'_2, \omega). \end{aligned} \tag{A.17}$$

In the case of cyclostationary fields, and using the Fourier series representation as in Eq. (2.7), the propagation law takes the form

$$\sum_n (\nabla_1^2 + k_1^2)(\nabla_2^2 + k_{2,n}^2)\tilde{C}_n(\mathbf{r}_1, \mathbf{r}_2, \omega)\delta(\Omega - n\omega_0) = \sum_n (4\pi)^2 \tilde{Q}_n(\mathbf{r}_1, \mathbf{r}_2, \omega)\delta(\Omega - n\omega_0), \tag{A.18}$$

where $\tilde{Q}_n$ are the generalized cross-spectra for the source and $\tilde{C}_n$ are the generalized cross-spectra of the field. By equating terms on each side of Eq. (A.18), one sees that each generalized cross-spectrum obeys the equation

$$(\nabla_1^2 + k_1^2)(\nabla_2^2 + k_{2,n}^2)\tilde{C}_n(\mathbf{r}_1, \mathbf{r}_2, \omega) = (4\pi)^2 \tilde{Q}_n(\mathbf{r}_1, \mathbf{r}_2, \omega), \tag{A.19}$$

where $k_{2,n} = (\omega + n\omega_0)/c$. Thus, for primary sources in free space, the cross-spectra away from the source can be found through the equation

$$\begin{aligned} \tilde{C}_n(\mathbf{r}_1, \mathbf{r}_2, \omega) &= \int \mathrm{d}^3 r'_1 \, \mathrm{d}^3 r'_2 \, \tilde{K}(\mathbf{r}_1, \mathbf{r}'_1, \mathbf{r}_2, \mathbf{r}'_2, \omega, \omega + n\omega_0) \\ &\times \; Q_n(\mathbf{r}'_1, \mathbf{r}'_2, \omega). \end{aligned} \tag{A.20}$$

In the case that the correlation function is needed only far from the source, one can make the so-called far-field approximation to the Green function in Eq. (A.20). This yields the

relationship

$$\tilde{C}_n(\mathbf{r}_1, \mathbf{r}_2, \omega) = \frac{e^{i(k_{2,n} r_2 - k_1 r_1)}}{r_1 r_2} \tilde{\mathcal{Q}}_n(-k_1 \hat{r}_1, k_{2,n} \hat{r}_2, \omega), \tag{A.21}$$

where $\tilde{\mathcal{Q}}_n$ is the six-dimensional spatial Fourier transform of $\tilde{Q}_n$.

In the case that the fields are also ergodic [for Eq. (A.5) and (A.16)] or cycloergodic [for Eq. (A.18)], then these ensemble averages can be related back to time-averaged measurements made with a detector.

REFERENCES

[1] P. B. Corkum and Z. Chang, "The attosecond revolution," *OPN*, vol. 19, no. 10, pp. 24–29, 2008.

[2] L. Mandel and E. Wolf, *Optical Coherence and Quantum Optics*. New York, NY: Cambridge University Press, 1995.

[3] E. Wolf, *Introduction to the Theory of Coherence and Polarization*. New York, NY: Cambridge University Press, 2007.

[4] N. Wiener, "Generalized harmonic analysis," *Acta Math.*, vol. 55, no. 1, pp. 117–258, 1930.

[5] A. Khintchine, "Korrelationstheorie der stationären stochastischen Prozesse," *Math. Ann.*, vol. 109, no. 1, pp. 604–615, 1934.

[6] A. Einstein, "Méthode pour la détermination de valeurs statistiques d'observation concernant des grandeurs soumises a des fluctuations irrégulières," *Arch. Sci. Phys. et Natur.*, vol. 37, pp. 254–256, 1914.

[7] G. Magyar and L. Mandel, "Interference fringes produced by superposition of two independent maser light beams," *Nature*, vol. 198, pp. 255–256, 1963.

[8] A. Papoulis, S. U. Pillai, A. Papoulis, and S. U. Pillai, *Probability, Random Variables, and Stochastic Processes*. New York, NY: McGraw-Hill, 1991.

[9] D. Vonderlinde, "Characterization of the noise in continuously operating mode-locked lasers," *Appl. Phys. B*, vol. 39, no. 4, pp. 201–217, 1986.

[10] H. A. Haus and A. Mecozzi, "Noise of mode-locked lasers," *IEEE J. Quantum Elec.*, vol. 29, no. 3, pp. 983–996, 1993.

[11] I. G. Fuss, "An interpretation of the spectral measurement of optical pulse-train noise," *IEEE J. Quantum Elec.*, vol. 30, no. 11, pp. 2707–2710, 1994.

[12] D. Eliyahu, R. A. Salvatore, and A. Yariv, "Noise characterization of a pulse train generated by actively mode-locked lasers," *J. Opt. Soc. Am. B*, vol. 13, no. 7, pp. 1619–1626, 1996.

[13] D. Eliyahu, R. A. Salvatore, and A. Yariv, "Effect of noise on the power spectrum of passively anode-locked lasers," *J. Opt. Soc. Am. B*, vol. 14, no. 1, pp. 167–174, 1997.

[14] D. A. Leep and D. A. Holm, "Spectral measurement of timing jitter in gain-switched semiconductor-lasers," *Appl. Phys. Lett.*, vol. 60, no. 20, pp. 2451–2453, 1992.

[15] D. E. Spence, J. M. Evans, W. E. Sleat, and W. Sibbett, "Regeneratively initiated self-mode-locked Ti-sapphire laser," *Opt. Lett.*, vol. 16, no. 22, pp. 1762–1764, 1991.

[16] J. Son, J. V. Rudd, and J. F. Whitaker, "Noise characterization of a self-mode-locked Ti-sapphire laser," *Opt. Lett.*, vol. 17, no. 10, pp. 733–735, 1992.

[17] D. E. Spence, J. M. Dudley, K. Lamb, W. E. Sleat, and W. Sibbett, "Nearly quantum-limited timing jitter in a self-mode-locked Ti-sapphire laser," *Opt. Lett.*, vol. 19, no. 7, pp. 481–483, 1994.

[18] M. Aoyama and K. Yamakawa, "Noise characterization of an all-solid-state mirror-dispersion-controlled 10-fs Ti-sapphire laser," *Opt. Commun.*, vol. 140, no. 4-6, pp. 255–258, 1997.

[19] A. Poppe, L. Xu, F. Krausz, and C. Spielmann, "Noise characterization of sub-10-fs Ti-sapphire oscillators," *IEEE J. Quantum Elec.*, vol. 4, no. 2, pp. 179–184, 1998.

[20] L. Xu, C. Spielmann, A. Poppe, T. Brabec, F. Krausz, and T. W. Hansch, "Route to phase control of ultrashort light pulses," *Opt. Lett.*, vol. 21, no. 24, pp. 2008–2010, 1996.

[21] D. J. Jones, S. A. Diddams, J. K. Ranka, A. Stentz, R. S. Windeler, J. L. Hall, and S. T. Cundiff, "Carrier-envelope phase control of femtosecond mode-locked lasers and direct optical frequency synthesis," *Science*, vol. 288, no. 5466, pp. 635–639, 2000.

[22] K. W. Holman, R. J. Jones, A. Marian, S. T. Cundiff, and J. Ye, "Intensity-related dynamics of femtosecond frequency combs," *Opt. Lett.*, vol. 28, no. 10, pp. 851–853, 2003.

[23] L. Matos, O. D. Mucke, J. Chen, and F. X. Kartner, "Carrier-envelope phase dynamics and noise analysis in octave-spanning Ti-sapphire lasers," *Opt. Express*, vol. 14, no. 6, pp. 2497–2511, 2006.

[24] V. Devrelis, M. O'Connor, and J. Munch, "Coherence length of single laser pulses as measured by CCD interferometry," *Appl. Opt*, vol. 34, pp. 5386–5389, 1995.

[25] V. M. Papadakis, A. Stassinopoulos, D. Anglos, S. H. Anastasiadis, E. P. Giannelis, and D. G. Papazoglou, "Single-shot temporal coherence measurements of random lasing media," *J. Opt. Soc. Am. B*, vol. 24, no. 1, pp. 31–36, 2007.

[26] R. A. Bartels, A. Paul, H. Green, H. C. Kapteyn, M. M. Murnane, S. Backus, I. P. Christov, Y. Liu, D. T. Attwood, and C. Jacobsen, "Fully spatially coherent EUV beams generated using a small-scale laser," *Science*, vol. 297, pp. 376–378, 2002.

[27] Y. Nagata, K. Furusawa, Y. Nabekawa, and K. Midorikawa, "Single-shot spatial-coherence measurement of 13 nm high-order harmonic beam by a Young's double-slit measurement," *Opt. Lett.*, vol. 32, no. 6, pp. 722–724, 2007.

[28] J. H. Eberly and K. Wodkiewicz, "The time-dependent physical spectrum of light," *J. Opt. Soc. Am*, vol. 67, no. 9, pp. 1252–1261, 1977.

[29] B. Cairns and E. Wolf, "The instantaneous cross-spectral density of non-stationary wavefields," *Opt. Commun.*, vol. 62, no. 4, pp. 215–218, 1987.

[30] S. A. Ponomarenko, G. P. Agarwal, and E. Wolf, "Energy spectrum of a nonstationary ensemble of pulses," *Opt. Lett.*, vol. 29, no. 4, pp. 394–396, 2004.

[31] H. Lajunen, J. Tervo, J. Turunen, P. Vahimaa, and F. Wyrowski, "Spectral coherence properties of temporally modulated stationary light sources," *Opt. Express*, vol. 11, no. 16, pp. 1894–1899, 2003.

[32] H. Lajunen, J. Tervo, and P. Vahimaa, "Overall coherence and coherent-mode expansion of spectrally partially coherent plane-wave pulses," *J. Opt. Soc. Am. A*, vol. 21, no. 11, pp. 2117–2123, 2004.

[33] H. Lajunen, P. Vahimaa, and J. Tervo, "Theory of spatially and spectrally partially coherent pulses," *J. Opt. Soc. Am. A*, vol. 22, no. 8, pp. 1536–1545, 2005.

[34] V. Torres-Company, H. Lajunen, and A. T. Friberg, "Effects of partial coherence on frequency combs," *J. Eur. Opt. Soc. - Rapid Pub.*, vol. 2, p. 07007, 2007.

[35] R. Gase and M. Schubert, "On the determination of spectral properties of non-stationary radiation," *J. Mod. Opt.*, vol. 29, no. 10, pp. 1331–1347, 1982.

[36] B. J. Davis, "Measurable coherence theory for statistically periodic fields," *Phys. Rev. A*, vol. 76, no. 4, p. 043843, 2007.

[37] R. W. Schoonover, B. J. Davis, R. A. Bartels, and P. S. Carney, "Optical interferometry with pulsed fields," *J. Mod. Opt.*, vol. 55, no. 10, pp. 1541–1556, 2008.

[38] R. W. Schoonover, B. J. Davis, R. A. Bartels, and P. S. Carney, "Propagation of spatial coherence in fast pulses," *J. Opt. Soc. Am. A*, vol. 26, no. 9, pp. 1945–1953, 2009.

[39] R. W. Schoonover, B. J. Davis, and P. S. Carney, "The generalized Wolf shift for cyclostationary fields," *Opt. Express*, vol. 17, no. 6, pp. 4705–4711, 2009.

[40] W. A. Gardner, A. Napolitano, and L. Paura, "Cyclostationarity: Half a century of research," *Signal Processing*, vol. 86, no. 4, pp. 639–697, 2006.

[41] J. J. Degnan, "Theory of the optimally coupled Q-switched laser," *IEEE J. Quantum Elec.*, vol. 25, no. 2, pp. 214–220, 1989.

[42] M. Horowitz, Y. Barad, and Y. Silberberg, "Noiselike pulses with a broadband spectrum generated from an erbium-doped fiber laser," *Opt. Lett.*, vol. 22, no. 11, pp. 799–801, 1997.

[43] T. Young, "The Bakerian lecture: Experiments and calculations relative to physical optics," *Phil. Trans. R. Soc. Lond*, vol. 94, 1804.

[44] T. P. Jannson, Ed., *Tribute to Emil Wolf: Science and Engineering Legacy of Physical Optics*. Bellingham, WA: SPIE Press, 2004.

[45] M. Born and E. Wolf, *Principles of Optics: Electromagnetic Theory of Propagation, Interference and Diffraction of Light*, 7th ed. New York, NY: Cambridge University Press, 1999.

[46] B. J. Davis, "Simulation of vector fields with arbitrary second-order correlations," *Opt. Express*, vol. 15, no. 6, pp. 2837–2846, 2007.

[47] S. Arahira, S. Oshiba, Y. Matsui, T. Kunii, and Y. Ogawa, "500 GHz optical short-pulse generation from a monolithic passively mode-locked distributed-bragg-reflector laser-diode," *Appl. Phys. Lett.*, vol. 64, no. 15, pp. 1917–1919, 1994.

[48] B. Davis, E. Kim, and J. R. Piepmeier, "Stochastic modeling and generation of partially polarized or partially coherent electromagnetic waves," *Radio Sci.*, vol. 39, no. RS1001, pp. 1–8, 2004.

[49] E. Wolf, "Invariance of the spectrum of light on propagation," *Phys. Rev. Lett.*, vol. 56, no. 13, pp. 1370–1372, 1986.

[50] E. Wolf, "Noncosmological redshifts of spectral lines," *Nature*, vol. 326, no. 6111, pp. 363–365, 1987.

[51] M. F. Bocko, D. H. Douglass, and R. S. Knox, "Observation of frequency shifts of spectral lines due to source correlations," *Phys. Rev. Lett.*, vol. 58, no. 25, pp. 2649–2651, 1987.

[52] E. Wolf, "Correlation-induced Doppler-type frequency shifts of spectral lines," *Phys. Rev. Lett.*, vol. 63, no. 20, pp. 2220–2223, 1989.

[53] N. A. Bahcall and R. M. Soneira, "The spatial correlation function of rich clusters of galaxies," *Astrophysical J. Part 1*, vol. 270, pp. 20–38, 1983.

[54] D. F. V. James and E. Wolf, "A class of scattering media which generate Doppler-like frequency shifts of spectral lines," *Phys. Lett. A*, vol. 188, no. 3, pp. 239–244, 1994.

[55] H. C. Kandpal, J. S. Vaishya, and K. C. Joshi, "Wolf shift and its application in spectroradiometry," *Opt. Commun.*, vol. 73, no. 3, pp. 169–172, 1989.

[56] A. Kubo, K. Onda, H. Petek, Z. Sun, Y. S. Jung, and H. K. Kim, "Femtosecond imaging of surface plasmon dynamics in a nanostructured silver film," *Nano Lett.*, vol. 5, no. 6, pp. 1123–1127, 2005.

[57] Y. H. Liau, A. N. Unterreiner, Q. Chang, and N. F. Scherer, "Ultrafast dephasing of single nanoparticles studied by two-pulse second-order interferometry," *J. Phys. Chem. B*, vol. 105, no. 11, pp. 2135–2142, 2001.

[58] T. H. Stievater, X. Li, D. G. Steel, D. Gammon, D. S. Katzer, D. Park, C. Piermarocchi, and L. J. Sham, "Rabi oscillations of excitons in single quantum dots," *Phys. Rev. Lett.*, vol. 87, no. 13, p. 133603, 2001.

[59] J. Reichert, R. Holzwarth, T. Udem, and T. W. Hänsch, "Measuring the frequency of light with mode-locked lasers," *Opt. Commun.*, vol. 172, no. 1-6, pp. 59–68, 1999.

[60] D. J. Jones, S. A. Diddams, J. K. Ranka, A. Stentz, R. S. Windeler, J. L. Hall, and S. T. Cundiff, "Carrier-envelope phase control of femtosecond mode-locked lasers and direct optical frequency synthesis," *Science*, vol. 288, no. 5466, p. 635, 2000.

[61] B. E. A. Saleh and M. C. Teich, *Fundamentals of Photonics.* New York, NY: Wiley-Interscience, 1991.

[62] S. Jacobs, "The optical heterodyne," *Electronics*, vol. 36, p. 29, 1963.

[63] A. E. Siegman, S. E. Harris, and B. J. McMurtry, "Optical heterodyning and optical demodulation at microwave frequencies," *Optical Masers*, vol. 54, no. 10, pp. 511–527, 1963.

[64] G. G. Stokes, "On the composition and resolution of streams of polarized light from different sources," *Trans. Cambr. Phil. Soc.*, vol. 9, p. 399, 1852.

[65] J. C. Maxwell, *A Treatise on Electricity and Magnetism.* New York, NY: Clarendon, 1892.

[66] W. C. Chew, *Waves and Fields in Inhomogeneous Media.* New York, NY: Springer, 1995.

[67] C. Tai, *Dyadic Green Functions in Electromagnetic Theory.* Piscataway, NJ: IEEE Press, 1994.

[68] D. F. V. James, "Change of polarization of light beams on propagation in free space," *J. Opt. Soc. Am. A*, vol. 11, no. 5, pp. 1641–1643, 1994.

[69] O. Korotkova, T. D. Visser, and E. Wolf, "Polarization properties of stochastic electromagnetic beams," *Opt. Commun.*, vol. 281, no. 4, pp. 515–520, 2007.

[70] R. W. Schoonover, A. M. Zysk, P. S. Carney, J. C. Schotland, and E. Wolf, "Geometrical optics limit of stochastic electromagnetic fields," *Phys. Rev. A*, vol. 77, no. 4, p. 43831, 2008.

[71] E. Wolf, "A macroscopic theory of interference and diffraction of light from finite sources. II. Fields with a spectral range of arbitrary width," *Proc. R. Soc. Lon. A*, vol. 230, no. 1181, pp. 246–265, 1955.

AUTHOR'S BIOGRAPHY

Robert W. Schoonover was born in Macomb, IL, on Halloween of 1981, and lived there through much of his childhood. He attended St. Paul Elementary School and Macomb Jr.-Sr. High School. In 2000, he began interning for Motorola and enrolled at the University of Illinois Urbana-Champaign (UIUC) to pursue a degree in electrical engineering. Upon graduation in 2004, UIUC beat out Motorola, and Robert enrolled in graduate school under the guidance of Prof. P. Scott Carney. In 2005, Robert won a Fulbright Scholarship to study at the Vrije Universiteit in The Netherlands under Prof. Taco Visser. Robert returned to UIUC in the summer of 2006 and completed his master's degree. He received a Ph.D. from the Delft University of Technology in May 2009. He is now a postdoctoral researcher at the Illinois Institute of Technology.